University of Groningen

# A synthetic RNA-based biosensor for fructose-1,6-bisphosphate that reports glycolytic flux

Ortega, Alvaro Darío; Takhaveev, Vakil; Vedelaar, Silke Roelie; Long, Yi; Mestre-Farràs, Neus; Incarnato, Danny; Ersoy, Franziska; Olsen, Lars Folke; Mayer, Günter; Heinemann, Matthias

*Published in:*
Cell Chemical Biology

*DOI:*
10.1016/j.chembiol.2021.04.006

**IMPORTANT NOTE: You are advised to consult the publisher's version (publisher's PDF) if you wish to cite from it. Please check the document version below.**

*Document Version*
Publisher's PDF, also known as Version of record

*Publication date:*
2021

Link to publication in University of Groningen/UMCG research database

*Citation for published version (APA):*
Ortega, A. D., Takhaveev, V., Vedelaar, S. R., Long, Y., Mestre-Farràs, N., Incarnato, D., Ersoy, F., Olsen, L. F., Mayer, G., & Heinemann, M. (2021). A synthetic RNA-based biosensor for fructose-1,6-bisphosphate that reports glycolytic flux. *Cell Chemical Biology*, *28*(11), 1554-1568.e8. [j.chembiol.2021.04.006]. https://doi.org/10.1016/j.chembiol.2021.04.006

**Copyright**
Other than for strictly personal use, it is not permitted to download or to forward/distribute the text or part of it without the consent of the author(s) and/or copyright holder(s), unless the work is under an open content license (like Creative Commons).

The publication may also be distributed here under the terms of Article 25fa of the Dutch Copyright Act, indicated by the "Taverne" license. More information can be found on the University of Groningen website: https://www.rug.nl/library/open-access/self-archiving-pure/taverne-amendment.

**Take-down policy**
If you believe that this document breaches copyright please contact us providing details, and we will remove access to the work immediately and investigate your claim.

*Downloaded from the University of Groningen/UMCG research database (Pure): http://www.rug.nl/research/portal. For technical reasons the number of authors shown on this cover page is limited to 10 maximum.*

Cell Chemical Biology

# A synthetic RNA-based biosensor for fructose-1,6-bisphosphate that reports glycolytic flux

## Graphical abstract

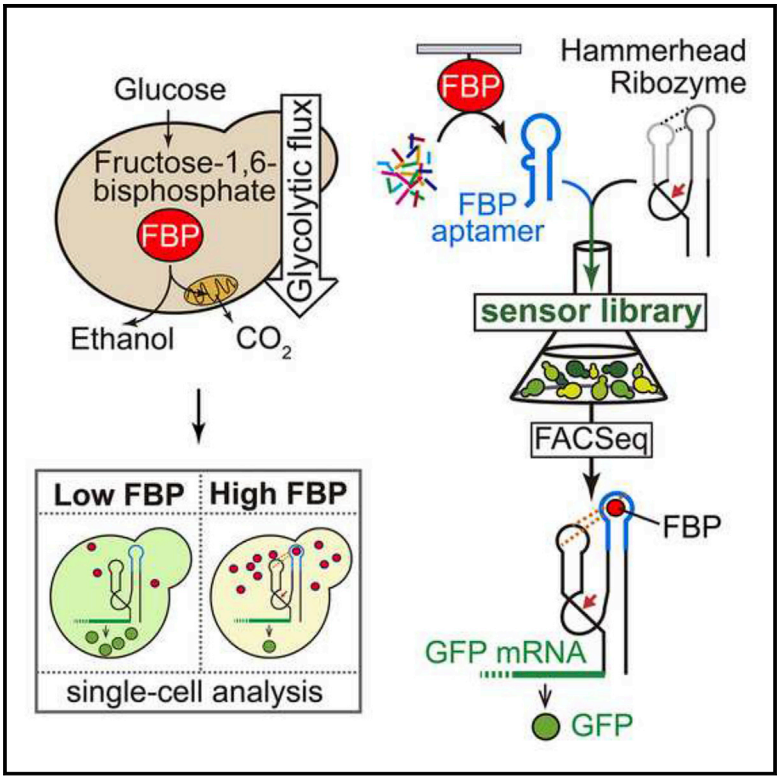


## Highlights

- RNA sensor for intracellular metabolite (FBP) developed from a synthetic aptamer
- Aptamer obtained that binds FBP in its intracellular concentration range
- *In vivo* screening of sensor libraries with the aptamer fused to a hammerhead ribozyme
- Developed sensor reports FBP in single cells and revealed metabolic heterogeneity

## Authors

Alvaro Darío Ortega, Vakil Takhaveev, Silke Roelie Vedelaar, ..., Lars Folke Olsen, Günter Mayer, Matthias Heinemann

## Correspondence

alvort05@ucm.es (A.D.O.), m.heinemann@rug.nl (M.H.)

## In brief

Current RNA sensors for intracellular metabolites employ aptamers from natural riboswitches. Ortega et al. developed a genetically encoded RNA sensor for fructose-1,6-bisphosphate to assess glycolytic flux in single cells. The study demonstrates the successful conversion of a synthetic aptamer for an endogenous metabolite into an RNA sensor.

Ortega et al., 2021, Cell Chemical Biology *28*, 1554–1568
November 18, 2021 © 2021 Elsevier Ltd.
https://doi.org/10.1016/j.chembiol.2021.04.006

CellPress

CellPress

Cell Chemical Biology

Article

# A synthetic RNA-based biosensor for fructose-1,6-bisphosphate that reports glycolytic flux

Alvaro Darío Ortega,[1,2,10,*] Vakil Takhaveev,[1,10] Silke Roelie Vedelaar,[1] Yi Long,[3,4,8] Neus Mestre-Farràs,[1,9] Danny Incarnato,[5] Franziska Ersoy,[3,7] Lars Folke Olsen,[4] Günter Mayer,[3,6] and Matthias Heinemann[1,11,*]

[1]Molecular Systems Biology, Groningen Biomolecular Sciences and Biotechnology Institute, University of Groningen, 9747 AG Groningen, the Netherlands

[2]Department of Cell Biology, Faculty of Biology, Complutense University of Madrid, 28040 Madrid, Spain

[3]LIMES Institute, University of Bonn, 53121 Bonn, Germany

[4]Institute of Biochemistry and Molecular Biology, University of Southern Denmark, DK5230 Odense M, Denmark

[5]Molecular Genetics, Groningen Biomolecular Sciences and Biotechnology Institute, University of Groningen, 9747 AG Groningen, the Netherlands

[6]Center of Aptamer Research & Development, University of Bonn, 53121 Bonn, Germany

[7]Present address: Institute of Food Chemistry, Gottfried Wilhelm Leibniz University Hannover, 30167 Hannover, Germany

[8]Present address: Medical Research Center, Southern University of Science and Technology Hospital, Shenzhen, Guangdong Province 518055, China

[9]Present address: Center for Genomic Regulation (CRG), The Barcelona Institute of Science and Technology, 08003 Barcelona, Spain

[10]These authors contributed equally

[11]Lead contact

*Correspondence: alvort05@ucm.es (A.D.O.), m.heinemann@rug.nl (M.H.)

https://doi.org/10.1016/j.chembiol.2021.04.006

## SUMMARY

RNA-based sensors for intracellular metabolites are a promising solution to the emerging issue of metabolic heterogeneity. However, their development, i.e., the conversion of an aptamer into an *in vivo*-functional intracellular metabolite sensor, still harbors challenges. Here, we accomplished this for the glycolytic flux-signaling metabolite, fructose-1,6-bisphosphate (FBP). Starting from *in vitro* selection of an aptamer, we constructed device libraries with a hammerhead ribozyme as actuator. Using high-throughput screening in yeast with fluorescence-activated cell sorting (FACS), next-generation sequencing, and genetic-environmental perturbations to modulate the intracellular FBP levels, we identified a sensor that generates ratiometric fluorescent readout. An abrogated response in sensor mutants and occurrence of two sensor conformations—revealed by RNA structural probing—indicated *in vivo* riboswitching activity. Microscopy showed that the sensor can differentiate cells with different glycolytic fluxes within yeast populations, opening research avenues into metabolic heterogeneity. We demonstrate the possibility to generate RNA-based sensors for intracellular metabolites for which no natural metabolite-binding RNA element exits.

## INTRODUCTION

Measuring the levels of intracellular metabolites is critical for a full understanding of cell physiology and pathology. Metabolite levels are now routinely measured at the scale of cell populations by mass spectrometry-based metabolomics (Johnson et al., 2016). However, the co-occurrence of cells with different metabolic phenotypes in the same cell population, i.e., metabolic heterogeneity (Schreiber and Ackermann, 2020; Takhaveev and Heinemann, 2018), is a level of complexity inaccessible to such techniques. Therefore, there is currently an unfulfilled requirement for methods that can probe intracellular metabolite levels at single-cell resolution. Such tools are urgently needed because cell-to-cell metabolic heterogeneity poses significant challenges in biotechnology as well as in cancer research (Delvigne et al., 2014; Kim and DeBerardinis, 2019; Rugbjerg and Sommer, 2019; Tasdogan et al., 2020).

Genetically encoded RNA-based metabolite sensors provide a promising avenue for measuring metabolite levels in single cells. However, there remain substantial challenges in the development of such reporters. RNA-based metabolite sensors use an RNA aptamer as a sensing domain that binds the target metabolite and an actuator domain that triggers a measurable signal; e.g., fluorescence. With the notable exception of an ADP sensor (Paige et al., 2012), all current RNA-based sensors for intracellular metabolites (Bose et al., 2016; Gao et al., 2014; Kellenberger et al., 2013, 2015; Lee and Oh, 2015; Paige et al., 2012; Su et al., 2016; Yang et al., 2013; You et al., 2015) use

sensing aptamers from natural bacterial riboswitches, which evolved optimal *in vivo* metabolite-binding affinity and conformational dynamics. On the other hand, for detecting xenobiotic compounds (such as theophylline, antibiotics, naringenin, or neurotransmitter precursors), also *in vitro* selected aptamers were utilized to generate RNA-based sensors (Bayer and Smolke, 2005; Boussebayle et al., 2019; Groher et al., 2018; Jang et al., 2017; Porter et al., 2017; Suess et al., 2003; Weigand et al., 2008). Thus, while it is possible in principle to select aptamers *in vitro* for any given metabolite, there has been remarkably little success in developing RNA-based sensors for endogenous intracellular metabolites for which no natural aptamer exists.

We conjecture that this is due to the challenges of merging a non-natural (i.e., *in vitro*-selected) sensing domain with an actuator domain, such as fluorogenic aptamers (e.g., Spinach) (Paige et al., 2012) or artificial riboswitches (Yang et al., 2013), into a functional biosensor. For instance, *in vitro*-selected metabolite-binding aptamers do not necessarily exhibit sufficient conformational changes to trigger actuator domains *in vivo*. Thus, an additional screening process might be necessary to obtain an *in vivo*-functional RNA sensor that effectively relays metabolite binding to the actuator domain. *In vivo* screening for xenobiotics is relatively straightforward as the target compound can be added to cell cultures at different concentrations, as is frequently done (Bayer and Smolke, 2005; Boussebayle et al., 2019; Groher et al., 2018; Jang et al., 2017; Porter et al., 2017; Suess et al., 2003; Weigand et al., 2008). By contrast, modulation of the intracellular concentration of an endogenous metabolite is highly challenging due to compensation by homeostatic mechanisms. This severely hampers the *in vivo* screening of sensors that use *in vitro*-selected aptamers. As a result, the development of synthetic RNA-based sensors for intracellular metabolites remains a largely unresolved problem.

In this work, we accomplished such a *de novo* development of an RNA-based device for the intracellular metabolite fructose-1,6-bisphosphate (FBP), a key glycolytic metabolite, for which no natural riboswitch has been discovered thus far. Specifically, we selected *in vitro* an aptamer that binds FBP under physiological conditions. Aptamer RNA-probing experiments then guided the rational design of an RNA-based regulatory device that consists of the FBP aptamer fused to a hammerhead ribozyme controlling GFP expression. Diverse libraries with variants of this RNA device were screened by fluorescence-activated cell sorting sequencing (FACS-seq), a dual-color fluorescence-based high-throughput method in yeast. This approach allowed us to visualize the output of thousands of these variants in response to different intracellular FBP concentrations, which we controlled through a combination of genetic and environmental perturbations. The identified FBP RNA-based sensor produces a ratiometric fluorescent output that reports the intracellular FBP concentration. Drawing on the across-kingdom correlation between the intracellular FBP concentration and the flux through glycolysis (Deutscher et al., 1995; Doan and Aymerich, 2003; Hackett et al., 2016; Huberts et al., 2012; Kochanowski et al., 2013; Litsios et al., 2017; Peeters et al., 2017; Zhang et al., 2017), we demonstrate by single-cell microscopic analyses that the FBP sensor can differentiate sub-populations with different glycolytic fluxes within clonal yeast cultures. By showcasing the conversion of an *in vitro*-selected aptamer into the RNA-based sensor for an intracellular metabolite, we lay the groundwork for future development of RNA-based devices with novel sensing specificities, which are necessary to ultimately tackle the issue of metabolic heterogeneity.

## RESULTS

### Selection of an FBP-binding RNA aptamer

To generate an FBP-sensing domain for our envisioned RNA device that reports intracellular FBP levels, and thus glycolytic flux, we first selected an FBP-binding RNA aptamer through systematic evolution of ligands by exponential enrichment (SELEX). After immobilizing FBP on epoxide-sepharose, we used an RNA library with the randomized region of 40 nucleotides flanked by constant regions of 15 and 25 nucleotides, respectively. To mimic the physiological conditions of the cytoplasm, we employed a phosphate buffer rich in $K^+$ and with a high concentration of glucose (to account for the presence of cytosolic metabolites) and added to it 5 mM $Mg^{2+}$ to facilitate the interaction of the doubly phosphorylated FBP with the anionic core of RNA (Ozalp et al., 2010). After 13 selection cycles, cloning, and sequencing, we obtained 10 different sequences, all of which showed a shortened variable region compared with the original library (Table S1), consistent with agarose gel electrophoresis analysis of the pools revealing a significantly reduced double-stranded DNA (dsDNA) length from selection round 9 onward (Long et al., 2016). Sequence analysis demonstrated highly similar clones, with an enriched motif, WUCCU, at the 5′ end of the variable region followed by a short nucleotide stretch (up to nine nucleotides), which allowed us to categorize the sequences into three sets (Table S1).

To assess the affinity and specificity of the selected clones to FBP, fluorescently labeled (CAL Fluor Red 610) RNA clones 34, 45, and 58 (i.e., representatives of each of the three sets of clones, Table S1) were incubated with sepharose columns with immobilized FBP, and then eluted with solutions of different FBP concentrations. We found that all clones bound FBP within the low millimolar concentration range (Figures 1A and S1E–S1G), which is the physiological concentration range of FBP in yeast (i.e., 0.2–8 mM) (Huberts et al., 2012; Monteiro et al., 2019). A mutant in the constant region that disrupted a stem structure predicted for these clones by Mfold energy minimization (nucleotide stretch C13 to A21, Figures S1A–S1D) required a 10-fold higher FBP concentration for elution (Figure 1A). Other phosphorylated intracellular metabolites (glucose-6-phosphate, fructose-6-phosphate, and ATP) failed to elute the RNA from the FBP column (Figures 1B and S1F–S1H). These results suggested that our selected clones are aptamers that selectively bind FBP in the physiological millimolar range. The fact that the clones C34, C45, and C58 displayed a similar affinity and selectivity (Figures 1A, 1B, and S1E–S1H) as well as all having a predicted structural stem-loop motif according to Mfold energy minimization (Figures S1A–S1C) suggested that the nucleotide sequence downstream the WUCCU motif (Table S1) is not essential for binding, indicating that the three clones are functionally equivalent. Thus, we continued our work with one clone, C45.

So far, we tested FBP binding to the aptamer when this compound was attached to sepharose. To delimit the concentration

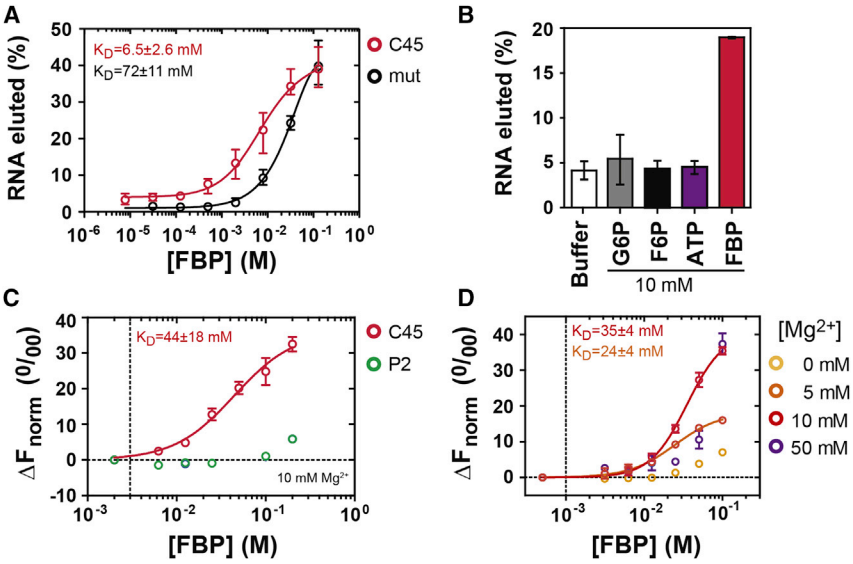


**Figure 1. The aptamer C45 binds FBP under physiological conditions**

(A) Binding assays of an RNA clone (C45) retrieved by SELEX and a mutant variant (mut), in which the stem structure predicted to exist in most selected clones is disrupted (Figures S1A–S1D). Fluorescently labeled (CAL Fluor Red 610) RNAs were incubated with FBP immobilized to sepharose, and eluted with different concentrations of free FBP.

(B) Assay done as in (A), but where 10 mM solutions of glucose-6-phosphate (G6P), fructose-6-phosphate (F6P), adenosine-triphosphate (ATP), or FBP were used to release RNA from a sepharose column with immobilized FBP. Fluorescence released by the last washing step before elution (buffer) is indicated.

(C) MST analysis of free FBP binding to Cy5-labeled C45 aptamer and a mutant lacking the 5′ and 3′-end tails and the four pair of nucleotides that make up the base of the conserved stem (P2) (Figure S2A). Binding assays were carried out in cytoplasmic buffer CB (See STAR methods) with 10 mM $MgCl_2$.

(D) MST analysis of FBP binding to C45 in solution under different $MgCl_2$ concentrations. Apparent dissociation constants ($K_D$) were estimated using a non-linear regression model assuming one binding site and specific binding with Hill slope. $K_D$ values correspond to binding assays carried out with 10 and 5 mM $MgCl_2$, respectively. In yeast, the intracellular free magnesium concentration is reported to be in the range from 0.1 to ~2 mM (Van Eunen et al., 2010; Zhang et al., 1997). Results in (A)–(D) represent the mean and the interquartile range from three replicates. Dashed lines in (C) and (D) indicate 0 in x and y axes. See also Figure S1.

range of free FBP required for binding to the aptamer, we used microscale thermophoresis (MST). Thermophoresis, the directed movement of a molecule in a temperature gradient, is altered in response to binding-induced changes in size, charge, or hydration shell of a labeled molecule, and allows the use of complex buffers and high concentrations of the ligand (Bley Folly et al., 2018). We tested FBP binding to Cy5-labeled C45 aptamer in the cytosolic buffer used for aptamer selection and found that C45 also bound free FBP in the millimolar concentration range. In contrast, a trimmed mutant lacking the 5′ and -3′-end tails and four nucleotide-pairs that make up the base of the conserved stem (P2) (Figure S2A) did not show any binding (Figure 1C). FBP binding was strongly dependent on the presence of $Mg^{2+}$ (Figure 1D), suggesting that $Mg^{2+}$ is necessary for proper C45 folding and/or for stabilizing the interaction with FBP. However, high FBP concentrations used in binding assays did not show any effect on RNA folding due to a potential $Mg^{2+}$ sequestering by the metabolite (Figures S1I and S1J), confirming that observed FBP-induced changes in C45 in MST denote FBP binding to C45. Together, these data show that we have identified an aptamer that selectively binds FBP in a $Mg^{2+}$-dependent fashion and within the physiological FBP concentration range.

## FBP binding alters the tertiary structure of C45 RNA aptamer

Toward unraveling the structural changes occurring in the C45 aptamer upon FBP binding, we performed 2′-hydroxyl acylation analyzed by primer extension (SHAPE) (Wilkinson et al., 2006) analyses, which, coupled with the RNAstructure energy minimization algorithm (Reuter et al., 2010), allowed us to generate an evidence-based model of the C45 secondary structure. The SHAPE reactivity patterns of the C45 nucleotides revealed a highly reactive core flanked by non-reactive regions predicted to fold as a stem-loop (Figure 2A, top panel), which matched the Mfold prediction solely based on energy minimization (Figure S1A). Specifically, the stem has 12 base pairs (C13–G26 and C36–G48) interrupted by a single mismatch (U16, U45) and a base bulge (U23), and the distal loop (L) contains nine nucleotides (U27–U35). The stem-loop structure is flanked by two single-stranded unstructured tails (Figure 2A, top panel).

To determine the structural changes upon FBP binding, we performed SHAPE also in the presence of a saturating concentration of FBP (86 mM). We found significant changes in the SHAPE reactivity in six of the nine residues in the distal loop (U28-A33) and in the bulge of the stem (U23), while the conserved WUCCU motif in P2 remained unchanged (Figure 2A, bottom panel). This result suggests that although the WUCCU motif does not seem to participate directly in ligand binding, it allows the formation of a stable stem that could be essential to maintain the overall structure of the aptamer, and thus of the FBP-binding site. As the RNAstructure model of the secondary structure remained the same as without FBP (Figure 2B), these FBP-induced changes in SHAPE reactivity most likely result from an altered tertiary structure of the aptamer.

To study the role of the distal loop and the bulge of C45 aptamer in FBP binding, we tested FBP binding to the aptamer variants in which these regions were mutated. In particular, we generated a mutant devoid of the bulge (U23, mutB) and a mutant where we substituted eight out of the nine nucleotides of the loop by their complementary counterparts (U27 to C34, mutL). These mutations did not impair the C45 structure as, according to Mfold energy minimization, mutB and mutL overall maintained the stem-loop secondary structure (Figures S2B and S2C), which we had found characteristic for the majority of the selected aptamer clones (Figures S2A–S2C, and results not shown). In MST analyses, we observed that mutL had an

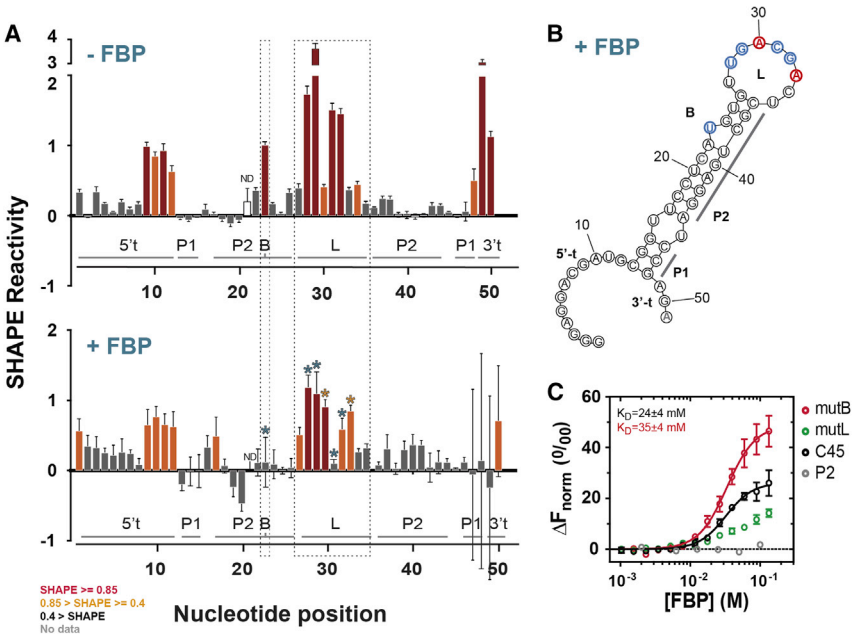


**Figure 2. C45 aptamer adopts a stem-loop secondary structure and, upon FBP binding, changes its tertiary structure, involving the loop**

(A) 1-Methyl-6-nitroisatoic anhydride (1M6)-SHAPE reactivity profiles of C45 aptamer in the presence (+FBP, bottom panel) or absence (−FBP, top panel) of FBP (86 mM). Bars represent the average of SHAPE reactivities of each nucleotide from five independent experiments; error bars represent the standard error of the mean. Bar colors are used to categorize SHAPE reactivity in three levels: dark gray for low, orange for intermediate, and red for high reactivity. SHAPE reactivity values ranges are indicated in the legend (bottom left). Asterisks indicate significant differences, where differences in reactivity were higher than 0.3 and p values from two-sided student's t test lower than 0.05; blue and red asterisks indicate a significant decrease or increase of SHAPE reactivity in the presence of FBP, respectively. Boxes with dotted lines delimit bulge (B) and loop (L) regions in C45 aptamer, where clustered differences in SHAPE reactivity occur. Different parts of the aptamer are indicated below the bars (5′t and -3′t, tails in 5′ and 3′ ends, respectively; P1, P2, stems 1 and 2; B, bulge; L, loop).

(B) Schematic representation of predicted C45 RNA secondary structure obtained with RNAstructure software, which considers energy minimization coupled to SHAPE reactivity. As in (A), blue and red indicate nucleotides showing a significant decrease or increase of SHAPE reactivity in the presence of FBP.

(C) MST analysis of FBP binding to mutants targeting the regions that altered SHAPE reactivity upon FBP binding: the U bulge (mutB: U23 deletion) and C45 loop (mutL: U27 to C34 substitution by its complementary sequence). C45 and mutant P2 (deletion of the base of the conserved stem: G1-U16 and U45-A51) show the extremes of the affinity to FBP. Apparent dissociation constants ($K_D$) were estimated using a non-linear regression model assuming one binding site and specific binding with Hill slope. Points represent the mean ± the interquartile range of three independent experiments. See also Figure S2.

impaired binding of FBP (Figure 2C), whereas the bulge deletion (mutB) only slightly decreased C45 affinity for FBP (Figure 2C), and preserved selectivity (Figure S2D), indicating that the bulge plays a less relevant role in FBP binding. Collectively, these results show that C45 folds as a stem-loop where FBP binding likely triggers tertiary-structure rearrangements of the aptamer involving the loop.

## An *in vivo* system to screen for RNA devices responding to intracellular FBP levels

To develop this *in vitro*-selected aptamer into an RNA device suitable for FBP sensing in yeast cells, we engineered a reporter system that allowed us to screen large RNA device libraries *in vivo*. To this aim, we had to couple the C45 aptamer with an actuator domain suitable to relay the FBP-triggered changes in the tertiary structure of the aptamer into a quantitative readout. Here, we employed the hammerhead ribozyme (HHRz) as an actuator domain because it has been shown to allow engineering RNA devices with ligand-responsive ribozyme tertiary interactions (Townshend et al., 2015). By integrating a C45-HHRz device into the 3′ UTR of a GFP-encoding mRNA, FBP binding to C45 would allosterically control HHRz self-cleaving activity, and thus GFP mRNA stability and protein expression (Figures 3A and S3A).

To correct for cell-to-cell variation in protein expression activity and for other extrinsic factors that may alter the readout of the reporter system, we used a centromeric plasmid, from which we not only expressed the HHRz-GFP construct but also mCherry without HHRz as an unregulated control (Figure S3B), as done recently (Townshend et al., 2015). Together, this system can report the activity of the HHRz via the mCherry-normalized GFP readout (GFP/mCherry ratio) in single yeast cells. To investigate the reporter system's dynamic range and resolution, we analyzed the readout of a set of mutants of HHRz (without the FBP aptamer included yet), which were recently shown to deliver different GFP/mCherry values (Townshend et al., 2015) (Method S1). We found that GFP/mCherry readout spanned over two logs, which enabled us to separate eight yeast clonal populations with different GFP/mCherry ratios without significant overlap (Figures S3B–S3D), indicating a broad dynamic range of the reporter system. Thus, we have implemented a reporter system in yeast that quantitatively relays HHRz activity to a GFP/mCherry readout, which is suitable for screening RNA devices with HHRz tertiary-structure-dependent activities.

For the screening, we next needed a strategy to modulate intracellular FBP concentrations. To this end, we used the engineered *Saccharomyces cerevisiae* strain *TM6**, which has only one chimeric hexose transporter (instead of the 17 of the wild-type [WT]) and thus displays a low glucose uptake rate and a low glycolytic flux (Elbing et al., 2004a). In contrast, when grown on maltose, which is transported into the cell with a different transporter, this strain has a high glycolytic flux, just like the WT (Litsios et al., 2019) (Figure 3B). Since glycolytic flux generally correlates with FBP levels (Hackett et al., 2016; Kochanowski et al., 2013; Litsios et al., 2017), we hypothesized that growing *TM6** cells in these two carbon sources could be utilized as the two extreme FBP conditions for screening. Quantitative targeted metabolomics demonstrated that FBP levels are on average about 9-fold lower in *TM6** grown on glucose compared with maltose (Figure 3C), reflecting a spread that nearly covers the physiological dynamic range of FBP (Huberts et al., 2012;

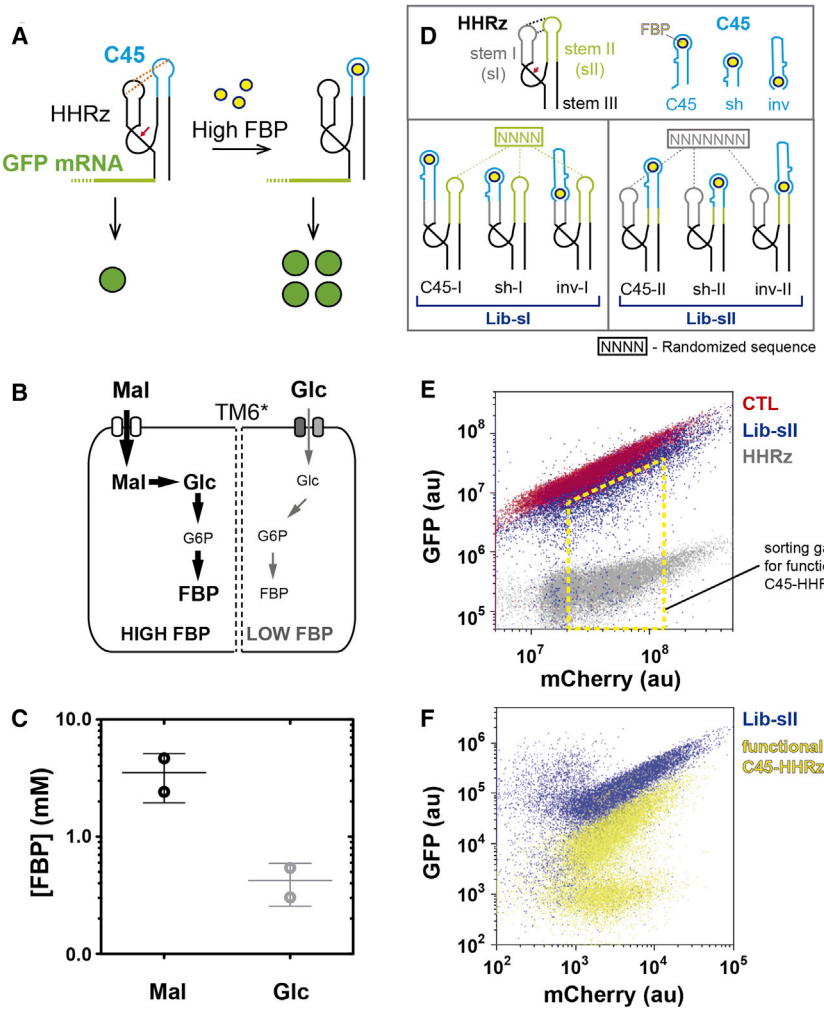


**Figure 3. An *in vivo* system to screen for RNA devices that respond to altered intracellular FBP levels**

(A) A reporter system that transduces intracellular FBP concentration into a fluorescent output. C45, the FBP-binding aptamer adopting a stem-loop secondary structure (blue), is grafted into the HHRz from the satellite RNA of tobacco ringspot virus at one of its stem-loops. Long-distance tertiary-structure interactions (dotted lines) are necessary to sustain self-cleaving activity of the ribozyme (red arrow). FBP binding at its high intracellular concentration distorts the tertiary-structure interactions, and hence inhibits HHRz activity. The C45-HHRz RNA device is cloned in the 3′ UTR of GFP. HHRz-mediated cleavage with low FBP levels leads to a short and unstable GFP mRNA, and thus to low expression of the protein (green circles). In contrast, when FBP levels are high, longer and more stable transcripts lead to higher GFP protein expression. The opposite mechanism of action can be also envisioned when FBP binding activates ribozyme activity. See also Figure S3, and Method S1.

(B) A system to modulate intracellular FBP concentrations to set screening conditions. *S. cerevisiae TM6** strain expresses only a chimeric hexose transporter that sustains a low glucose uptake rate, and thus a low glycolytic flux (right) and low FBP levels, when glucose is provided (Litsios et al., 2019). Maltose is taken up normally, leading to a high glycolytic flux and thus high FBP level.

(C) Metabolomic analysis of intracellular FBP concentration in *TM6** yeast cells cultured in minimal medium with either maltose or glucose as the sole carbon source. FBP abundance was obtained from two independent experiments and two determinations per experiment. Cell volume was determined for at least 70 cells per sample. Lines represent the mean of the two experiments ±standard deviation (SD).

(D) Design of the C45-HHRz RNA device library. We refer the reader to Figure S4 to obtain a full description and details of the constructs on the primary sequence level. C45 aptamer was grafted into either of the two stem-loops of HHRz (stem I and II, gray and green, respectively) using three different strategies: (1) the loop of the receiving stem in HHRz is removed and C45 placed next to the HHRz stem in a direct (C45-I, C45-II) or (2) inverted orientation (invI, invII), and (3) the HHRz loop is removed and a shortened version of C45 merged with the HHRz stem (sh-I, sh-II). The sequence of the opposite HHRz loop (that is, the loop I when C45 is grafted into stem II, and vice versa) is randomized (gray and green N stretches) to generate a library. Out of it, we select those clones that establish interactions between C45 and the opposite HHRz stem-loop, and therefore sustain the HHRz activity. Lib-sI and Lib-sII are the libraries made by equimolar pooling of the libraries C45-, sh- and inv, -I and -II.

(E) Sorting of RNA devices with residual HHRz activity in the Lib-sII C45-HHRz library. GFP-mCherry scatterplot where Lib-sII library (blue), along with RNA device controls containing fully active (HHRz, gray) and inactive HHRz (CTL, Red) are overlaid. The sorting gate (yellow dotted polygon) used to collect C45-HHRz RNA devices with functional HHRz is indicated.

(F) Comparison of the initial cellular Lib-sII library and the sorted population enriched in C45-HHRz devices with functional ribozyme. In (E) and (F), 20,000 cells from each population are plotted. Identifiers of the populations plotted are indicated on the right side of each plot. Fluorescence arbitrary units shown in (E) and (F) are different because sorting (E) and ulterior analysis after re-growth of the sorted population (F) were done in different devices. For simplicity, sorting and post-growth analysis of sorted population are shown only for Lib-sII. See also Figure S5.

Kochanowski et al., 2013). Thus, by growing the *TM6** strain on two different carbon sources, we could control FBP levels within its physiological range, and therefore we could use this system to screen *in vivo* for RNA devices responding to physiological FBP concentration changes.

## Design and pre-selection of C45-HHRz RNA devices with a functional ribozyme

To identify RNA devices with an FBP-dependent ribozyme activity, we next constructed the libraries of HHRz-C45 RNA devices where we grafted the C45 aptamer into one of the two HHRz stem-loops (I or II) involved in tertiary interactions required for self-cleavage (Townshend et al., 2015). FBP binding would then disrupt tertiary interactions between the C45 aptamer's loop and the opposite stem-loop of the ribozyme. Here, either the HHRz stem-loop I could receive the aptamer to interact with the stem-loop II, or vice versa (Figure 3A). However, grafting the aptamer into an HHRz stem-loop itself may distort HHRz structure, thereby rendering the ribozyme inactive irrespective of FBP binding.

To increase the chances of maintaining residual ribozyme activity after aptamer integration and to mitigate a potential structural bias of using a single grafting strategy, we introduced the FBP aptamer into either the stem-loop I (Figures S4A–S4C) or II (Figures S4D–S4F), each with three different strategies (Figure 3D). In the first strategy, we removed the HHRz loop and appended C45 to the remainder of the stem (the receiving stem) in the same orientation (C45, Figures S4A and S4D). In the second strategy, we did the same but just inserted C45 in the inverted orientation (inverted [inv], Figures S4C and S4F). In the third strategy, we replaced the whole HHRz stem-loop by a version of the FBP aptamer containing a shortened stem (sh, Figures S4B and S4E). With these three integration strategies, we generated combinatorial libraries of the RNA devices in which the HHRz loop sequence of the stem-loop opposite to the receiving stem was randomized: four nucleotides of loop II when the receiving stem was stem I, and seven nucleotides of loop I when the receiving was stem II (Figures 3D and S4). The libraries generated with these three different C45-integration strategies in each of the two stems I and II were pooled and transformed into yeast, resulting in two C45-HHRz RNA device libraries (Lib-sI and Lib-sII, Figure 3D) with theoretical sizes of 768 and 49,152, respectively.

From these two C45-HHRz libraries, we next selected RNA devices in which the ribozyme was still functional after C45 insertion as only those with residual ribozyme activity are suitable for later screening for FBP-dependent regulation of that activity. To this aim, we used FACS to collect those clones in the libraries with low GFP expression at the low-FBP condition (i.e., in glucose-grown *TM6** cells) (Figure 3E) because then RNA devices should be mainly in their FBP-unbound state, and thus with unperturbed basal HHRz activity. We defined the reference points for non-self-cleaving activity and maximal self-cleaving activity with two of the HHRz-GFP constructs used for the calibration of the reporter system (without C45): the inactive HHRz (CTL, Figures S3B–S3D) and WT ribozyme (HHRz, Figures S3B–S3D). Here, we found that more than 95% of the clones in the C45-HHRz libraries had a non-functional HHRz, with GFP/mCherry ratio overlapping with that of the CTL inactive mutant (Figure 3E). Then, we sorted the cells that had GFP/mCherry ratio lower than in the CTL mutant, thus collecting RNA devices with a functional ribozyme (Figure 3E). Sanger sequencing before and after sorting revealed a reproducible change of the sequence pattern in the randomized region (data not shown), confirming the enrichment of particular sensor variants based on its ribozyme's functionality. By preselecting C45-HHRz RNA devices with a residual ribozyme activity, we enriched the library in clones suitable for screening, thereby enhancing the chances to identify RNA devices with FBP-dependent regulation.

Next, we wondered which of the three aptamer grafting strategies and which sequence features in the randomized loop would preserve HHRz activity. Through next-generation sequencing (NGS) of the pre-selected populations, we found that active C45-HHRz devices predominantly contained the *inv* aptamer in either of the HHRz stems, and the shortened aptamer replacing the whole HHRz stem-loop I (*sh*) (Figure S5D). The prevalence of *sh* variants in stem I within the active devices could be connected with the fact that stem I is naturally longer compared with stem II and, therefore, its replacement by the aptamer having a comparable length might have less impact on the ribozyme structure (compare Figures S4B and S4E). Considering also that, in *inv* variants, the length of the receiving stem is not altered (Figures S4C and S4F), these results suggest that the length of the stem into which the aptamer is grafted is a critical factor for ribozyme functionality.

Finally, the analysis of the sequences of the HHRz loop opposite to the aptamer-receiving stem in the active HHRz variants revealed an enrichment of A and G in stem-loop II, and a high conservation of A in the fourth position when the shortened C45 was inserted in place of stem-loop I (*sh-I*) (Figure S5D). On the contrary, when C45 was inserted in place of stem-loop II, we found an overrepresentation of G and T in the randomized region of the stem-loop I. Interestingly, C was observed underrepresented in the randomized region of either stem-loop (Figure S5D). These features preserving ribozyme activity could be utilized in the generation of new, doped C45-HHRz libraries with a higher fraction of functional ribozymes to increase screening effectiveness.

At this point, we have generated an RNA device library with multiple FBP aptamer integration strategies from which we collected the variants with residual ribozyme activity, which is a requirement for the next step; i.e., to identify the variants where FBP levels influence this activity.

## High-throughput *in vivo* screening of RNA devices that report intracellular FBP

To identify C45-HHRz clones with an FBP-dependent readout, we implemented a high-throughput approach that examines the mCherry-normalized GFP expression of thousands of C45-HHRz variants simultaneously in a single experiment, previously referred to as FACS-seq (Townshend et al., 2015). Globally, our approach entailed four steps. First, we pooled the two libraries containing the functional C45-HHRz devices (c.f. Figure 3F) into a single population (called input from now on), which was then grown in either the high or low intracellular FBP conditions; i.e., *TM6** cells cultivated in either maltose or glucose, respectively (Figure 4A, growth). Second, we sorted the cells of the input library into six sub-populations according to the cells' GFP/mCherry expression ratios (Figure 4A, cell sorting). Third, after identifying all clones in each sorted sub-population by NGS and inspecting each clone's frequencies, we assigned a single GFP/mCherry ratio value ($\mu_i$ hereafter) to every C45-HHRz variant when grown in either condition (Figure 4A, *NGS*). Finally, analyzing the distributions of $\mu_i$, we identified the clones that respond to the difference between the high and low intracellular FBP conditions.

To sort the C45-HHRz variants, we defined six bins on the basis of GFP/mCherry ratio. To this end, we first set the upper and lower limits of GFP/mCherry ratio to the readouts of the CTL inactive mutant (maximal GFP/mCherry ratio) and of the HHRz WT sequence (minimal ratio) (Figure S6A), thereby defining the boundaries of the readout's dynamic range. Then, we split this range into six non-overlapping bins whose width was set to the size of the dispersion of GFP and mCherry signals (or intrinsic noise) in clonal populations (Figures 4B and S6A). With these settings, for both the low- and the high-FBP conditions, the sorting yielded six sub-populations with barely overlapping GFP/mCherry expression profiles that were stably maintained over

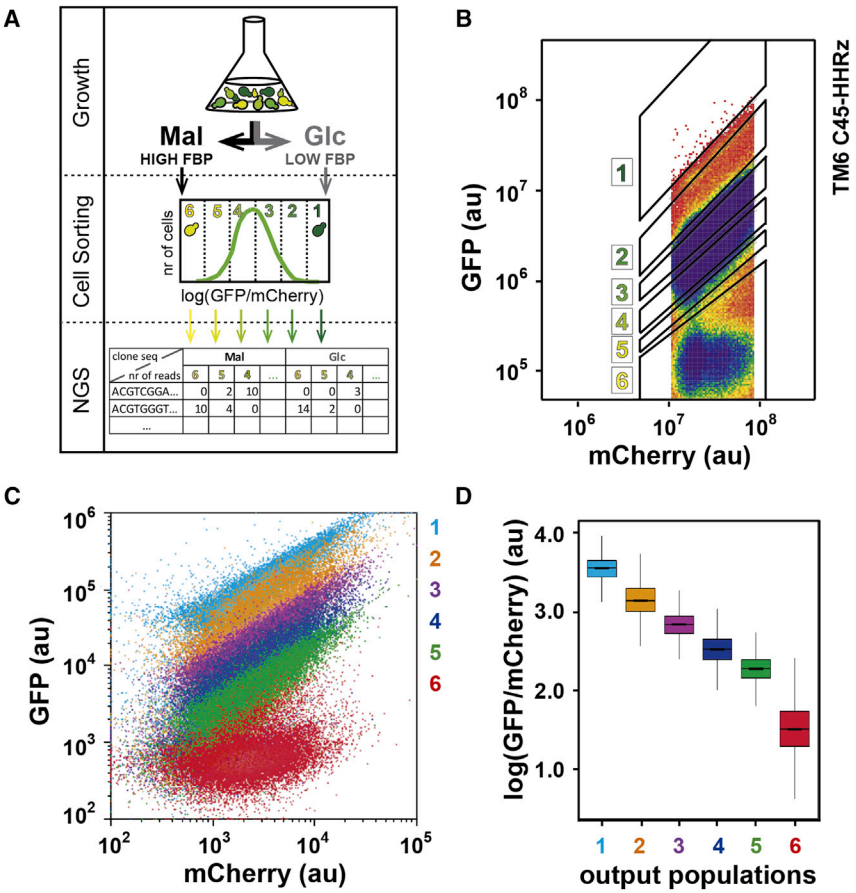


**Figure 4. Sorting of C45-HHRz RNA device library yields six sub-populations with distinct GFP/mCherry ratios**

(A) Experimental pipeline of the high-throughput *in vivo* screening of C45-HHRz RNA devices that respond to FBP. *TM6** cells with the C45-HHRz library are grown in medium with either glucose or maltose (top panel). Cells are sorted into six sub-populations according to their GFP/mCherry ratios (middle panel). Sorted cells sub-populations are subjected to NGS to identify the distribution of each clone throughout the population.

(B) Sorting of C45-HHRz RNA device library. A representative example of the gating of a FACS-seq sorting experiment is shown (C45-HHRz library grown in glucose; 378,309 cells plotted). Cells with an intermediate 1-log-wide mCherry expression were gated. We used this gating because we found that the GFP signal was less robust in cells with low mCherry expression in clonal populations (c.f. GFP-mCherry signal overlap among different HHRz versions for mCherry values between $5 \times 10^5$ and $5 \times 10^6$ in Figure S6A), while in cells with intermediate mCherry levels dispersion of GFP values remained constant across the bins (Figure S6B). Sorting gates were established according to GFP/mCherry ratio, ranging from the signal of fully active (gate 6) to that of inactive ribozymes (gate 1). The width of the gates 2–5 was set according to the width of a cell population from a single clone in GFP/mCherry plot. See also Figure S6.

(C) Overlay of GFP-mCherry scatterplots obtained from regrown, sorted sub-populations. Sorted sub-populations were grown for several generations prior to analysis; 20,000 cells from each sub-population are plotted.

(D) Single-cell GFP/mCherry ratio distribution in sorted sub-populations from C45-HHRz library calculated from experiment shown in (C). The boxes show the interquartile range with the median in the middle, and the whiskers spanning from the 1st to 99th percentile.

generations (Figure 4C). The single-cell GFP/mCherry distribution of all sub-populations evenly covered the readout's dynamic range (i.e., without gaps with underrepresented values or with peaks of over-represented values) spanning more than three logs (Figure 4D). These results demonstrated that we could sort the clones of our input library into sub-populations with distinct and stable GFP/mCherry values.

Next, we used NGS to identify the C45-HHRz variants and to determine their respective frequencies in each sub-population. We utilized the variants' frequencies in every sub-population together with the fraction of the input population that was sorted to each bin in the sorting experiment to reconstruct each variant's distribution across the bins (Table S2). The sum of these reconstructed absolute frequencies across the bins for every variant significantly correlated with the variants' frequencies in the unsorted input population, indicating that our sampling method, based on GFP/mCherry-ratio-guided population binning, produced a fair representation of the entire population (Figure S7A). To determine $\mu_i$ of each variant, the medians of cells' GFP/mCherry ratio in the bins (determined in each sorting experiment) were weighted by the distribution of the variant across the bins (Table S2). The robustness of determining $\mu_i$ values was demonstrated by a strong correlation between two replicate experiments (Figure S7B). Through this procedure, we could assign a $\mu_i$ value for each intracellular FBP condition to 15,031 unique C45-HHRz variants (covered by four or more reads in two independent sorting experiments, Methods S2 and S3).

To identify clones with significantly different $\mu_i$ values between the conditions of low and high intracellular FBP, we defined the response of the sensor, $D_i$, a new variable that corresponds to the logarithm of the quotient between the $\mu_i$ of a clone in the two FBP condition: $D_i = lg \frac{\mu_i^{Glc}}{\mu_i^{Mal}}$ (Table S2). The analysis of the distribution of this response variable revealed 63 clones (0.42% of all screened clones) that consistently showed an extremely high or low $D_i$ value (i.e., outliers) in two replicate experiments (Figure 5A, Method S3). Thus, these 63 clones showed a condition-dependent change (either increase or decrease) in $\mu_i$ indicative of an FBP-dependent response (resembling either on or off sensors).

In the screening experiments, we perturbed the intracellular FBP levels by changing the carbon source on which *TM6** cells grew (low FBP on glucose and high FBP on maltose, Figure 3C). To sort out clones that might respond to unknown carbon-source-related changes aside from FBP-level differences, we next screened the C45-HHRz library also in WT cells. In contrast

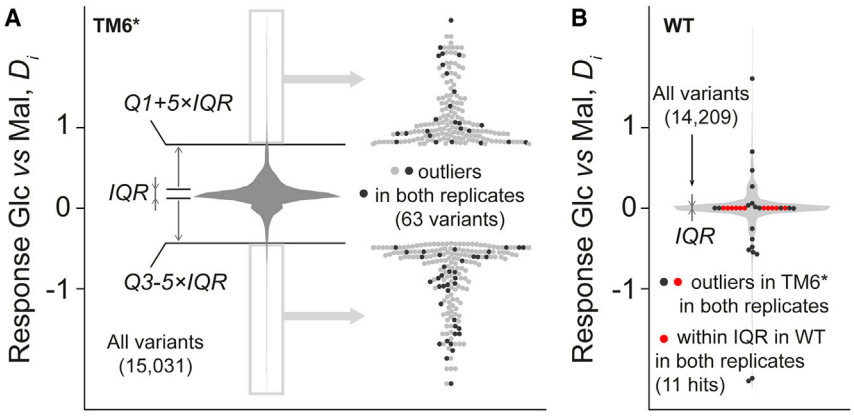


**Figure 5. Hit selection in high-throughput *in vivo* screening of C45-HHRz variants that respond to differences of intracellular FBP**

(A) Identification of variants in C45-HHRz library expressed in the *TM6** strain that have different response while growing on glucose versus growing on maltose, associated with low and high intracellular FBP, respectively. To compare a variant's response to the change in intracellular FBP, we calculate the measure Response Glc versus Mal, $D_i$ (y axis; see Table S2 for details), a transformed measure of the change in the GFP/mCherry ratio ($\lg \mu_i^{Glu}/\mu_i^{Mal}$), and check if its value deviates from those of other variants. The distribution of this response $D_i$ of all the variants is depicted in the violin plot. We select variants with the extreme response values that are located beyond the segment $[Q1 - 5 \cdot IQR,\ Q3 + 5 \cdot IQR]$ (gray boxes on the left, gray and black dots on the right), where $Q1$ and $Q3$ are the lower and upper quartiles, and $IQR$ is the interquartile range. To exclude variants that end up in the selection due to technical noise, we repeated the sorting experiment and looked for clones with consistently deviating response (63 clones, black dots on the right). All the clones in this analysis are covered by four sequencing reads or more in each of the four sorting experiments (2 carbon sources × 2 independent experiments).

(B) Exclusion of variants showing an intracellular FBP-independent response. WT cells display a similar FBP level when cultured in glucose or in maltose, and, thus, hits should not show a response between these carbon sources in C45-HHRz library expressed in WT background. Eleven variants are located within the $IQR$ of the response in C45-HHRz library in the WT in two independent sorting experiments, these variants are thus considered the hits from the screening. The presented distribution and its $IQR$ used for selection is calculated from the data of variants supported by four sequencing reads or more in each of the four sorting experiments; the values corresponding to the dots were obtained using the data supported by at least two reads in each of the four sorting experiments. For simplicity of the representation, in both (A) and (B), we present the data corresponding to one replicate experiment (R1). See Method S3 describing the hit selection in more detail, and Figure S7.

with *TM6**, WT cells grown in glucose and maltose have nearly identical glycolytic rates, and thus FBP levels (Huberts et al., 2012). Therefore, an ideal FBP-responding candidate should have different $\mu_i$ values in glucose and maltose in *TM6** but identical values in the WT (where on both carbon sources FBP levels are high). Here, we found that, out of the 63 strongly responding clones identified with *TM6** (Figure 5A), 11 had the response $D_i$ around 0 in the WT (Figure 5B). Thus, our *in vivo* screening led to the discovery of 11 hits showing FBP-dependent changes in the GFP/mCherry ratio readout.

### *In vivo* FBP binding is essential for sensor functionality

To validate the hits as intracellular FBP sensors, we expressed them in the *TM6** and WT strains, and analyzed their GFP/mCherry ratios in clonal populations grown on either maltose or glucose, which lead to different intracellular FBP concentrations in *TM6** but not in the WT. We found that nine out of ten tested hits had different readouts in the conditions of high and low intracellular FBP in *TM6**, while they had the same readout in two high-FBP conditions in the WT (Figure 6A), indicating that these hits exhibit an FBP-dependent response. A random variant not identified as a hit in the high-throughput screening, carried along here as a control, responded neither in *TM6** nor in the WT (control 1_10, Figure 6A). These experiments validated the FBP-dependent response of nine of the hits identified in the screening.

To confirm the specificity in the observed FBP-dependent response, we mutated the C45 aptamer in some validated hits. Drawing on our finding that FBP binding is impaired *in vitro* when the aptamer's loop is mutated (Figure 2C, *mutL*), we generated *mutL* versions of C45 in three validated hits. For hit 3_7, we found that the mutated and non-mutated versions showed a similar response between the conditions of high and low FBP in *TM6** (Figures 6B and 6C), disproving that FBP binding triggers the observed change in the GFP/mCherry ratio. However, the *mutL* versions of the other tested hits (4_1m and 2_6m) lost the FBP-dependent change of the readout (Figures 6B and 6C), demonstrating that in 4_1 and 2_6 FBP binding to C45 is essential for the observed response, confirming that these are FBP sensors. The sensor 4_1 belongs to the C45-II design of C45-HHRz RNA device, and the sensor 2_6 has the inv-II design (Figure 3D).

Focusing on the developed sensor 2_6 with the biggest amplitude of the readout (Figures 6A and 6B, 2_6), we investigated the sensor's response to different intracellular FBP concentrations between the extreme levels employed in the high-throughput screening. For this, we exploited the *HXT7*, *TM3*, and *TM4* strains, which were previously shown to have different glucose uptake rates and glycolytic fluxes located between the respective values of the WT and *TM6** strains used so far (Elbing et al., 2004a). Here, we found that, across the five strains, the GFP/mCherry ratios of the sensor were markedly different and negatively correlated with intracellular FBP concentrations (Figure 6D). On the contrary, the GFP/mCherry ratios from the mutated sensor with impaired FBP binding did not markedly change with different intracellular FBP concentrations (Figure 6E). Thus, the sensor 2_6 displays a dynamic range that covers various FBP concentrations observed *in vivo*.

We next wondered about the RNA structural elements relevant for sensor functionality *in vivo*. To this end, we performed *in vivo* RNA structural probing in which cells expressing the sensor 2_6 were treated with dimethyl sulfate (DMS) followed by targeted dimethyl sulfate (DMS) mutational profiling with sequencing (DMS-MaPseq) analysis (Zubradt et al., 2017). Here, we found

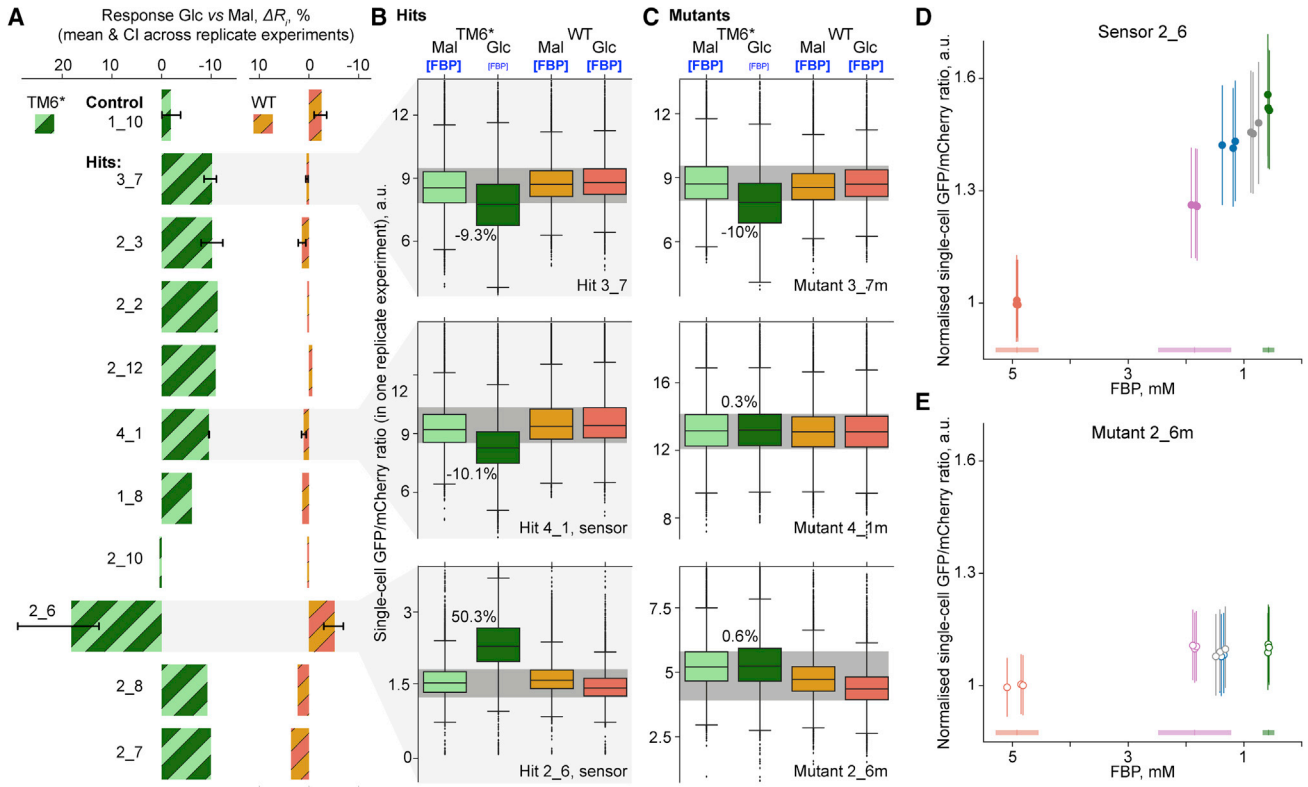


**Figure 6. Validation of individual hits as FBP sensor candidates**

(A) Response of hits in cells cultivated in glucose compared with cells cultivated in maltose (Response Glc vs Mal, $\Delta R_i$). Intracellular FBP concentration differs in *TM6** strain and stays the same in the WT strain, when cells are grown on these two carbon sources (Glc, glucose; Mal, maltose). Response Glc vs Mal, $\Delta R_i$, is calculated as the percentage of the change in the GFP/mCherry ratio between the cells cultivated in glucose and maltose compared with the cells cultivated in maltose: $\Delta R_i = \frac{1}{|G|} \cdot \sum_{t \in G} \frac{M(i,Glc,t) - M(i,Mal,t)}{M(i,Mal,t)} \cdot 100\%$, where $i$ is a hit; $M(i, Glc, t)$ and $M(i, Mal, t)$ are the median GFP/mCherry ratios in the population of cells grown on glucose and maltose, respectively; $G$ is the set of three ($|G|$) time points $t$ in the exponential part of a culture's growth curve. The bar and whisker lengths denote the mean value of $\Delta R_i$ and its 95% confidence interval calculated for the replicate cultivation experiments. No whiskers are shown in the case of single cultivation experiment. The following numbers of data points were used to calculate the mean and the confidence interval in both TM6* and WT: six for 1_10 in both strains, three for 3_7, two for 2_3, three for 4_1, and three for 2_6.

(B and C) The single-cell distribution of the GFP/mCherry ratio in the four populations (2 strains × 2 carbon sources) at one time point $t$ in the growth curves of selected hits (B) and their mutants (C). The box shows the interquartile range *IQR*, the line in the center of it denotes the median $M(i, Mal, t)$ or $M(i, Glc, t)$, the whiskers spread until $Q1 - 1.5 \times IQR$ or $Q3 + 1.5 \times IQR$, where $Q1$ and $Q3$ are the lower and upper quartiles. The percentage between the distributions of maltose- and glucose-grown TM6* populations is the value of the ratio $\frac{M(i,Glc,t) - M(i,Mal,t)}{M(i,Mal,t)} \cdot 100\%$, which contributed to the calculation of the response variable $\Delta R_i$ in case of hits (A). The dark-gray horizontal band denotes the central tendency of the values of the GFP/mCherry ratio associated with high intracellular FBP, with the upper and lower boundaries being the maximal upper quartile and the minimal lower quartile across the populations of TM6* on maltose, WT on maltose and glucose. To build each of the boxplots, from 15,786 to 18,729 single-cell values were used.

(D and E) The dependence of the GFP/mCherry ratio of the sensor 2_6 (D) and its mutant 2_6m with impaired FBP binding (E) on the intracellular FBP concentration varying across strains with different glucose uptake rates and glycolytic fluxes (Elbing et al., 2004a). Five strains shown in different colors (from left to right: WT, *HXT7*, *TM3*, *TM4*, and *TM6**) were cultivated on glucose in three replicate batch cultures. For every replicate culture, the median and interquartile range (IQR) of single-cell GFP/mCherry ratios are presented as a circular marker and thin vertical line, respectively. To normalize the sensor and mutant readouts, we divided single-cell GFP/mCherry ratios by the average of the medians in three replicate WT cultures (1.44 for the sensor and 4.54 for the mutant). To calculate the medians and IQRs, we used from 23,474 to 86,554 cells analyzed in flow cytometry. The intracellular FBP concentrations of the WT, *HXT7*, and *TM6** strains as previously measured in Schmidt (2014) are summarized via the mean ± SD of replicate cultivations and shown as tick horizontal lines at the bottom of the plots. The estimation of the FBP concentration in the replicates and strains yielding GFP/mCherry ratios is described in the STAR methods.

that the DMS-reactivity pattern is consistent with the expected formation of stem-loop I and a long stem with an internal loop, which is a product of merging HHRz stem II and the aptamer C45 (Figures 7A and 7B; Figure S4F). Zooming in on the aptamer region in the RNA device, we further found that, although some nucleotides involved in the loop *in vivo* (Figure 7B, U39–C42, U64–U66) are *in vitro* related to the stem (Figure 2B, G37–C38, U23–U25), the biggest part of the grafted aptamer (Figure 7B, U43–A63) has the same stem structure *in vivo* as determined *in vitro* (Figure 2B, C13–A22, U39–G48). In particular, we observed that the P1 sequence and the WUCCU motif (Figure 7B, U57–U61) constitute the stem also *in vivo*, identically to most *in vitro*-selected FBP-binding aptamer clones (Figures S1A–S1C; results not shown). Supporting the importance of C45 aptamer folding into this stem observed both *in vitro* and *in vivo*, DMS-structural probing of the FBP-unresponsive mutant 2_6m

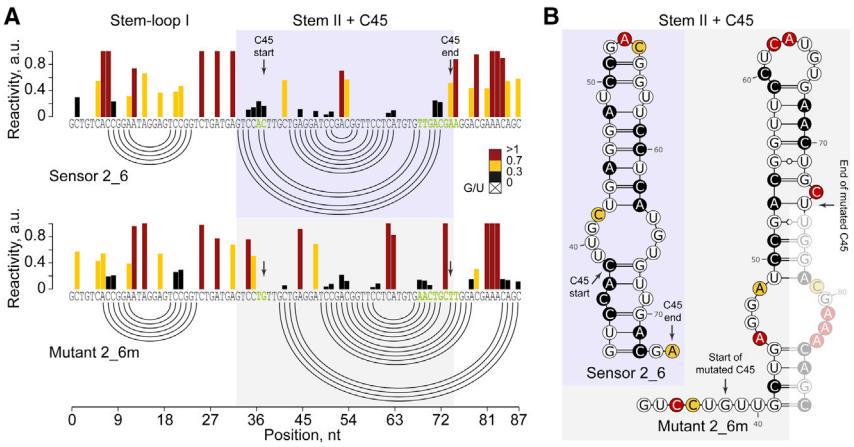


**Figure 7. The intracellular FBP sensor *in vivo* maintains the structural elements of the C45 aptamer that are critical for FBP binding *in vitro***

(A) *In vivo* DMS-MaPseq analysis of the C45-HHRz RNA device in the sensor 2_6 and its mutant 2_6m. Bases differing between the two sequences are highlighted in green. Bars are color coded according to base reactivity (low, black; medium, yellow; high, red; G and U do not show reactivities). Mutational data have been normalized by box-plot normalization. Reactivities were capped at 1 for representation purposes. Experimentally constrained secondary structures are depicted as arc plots.

(B) Secondary structure models of Stem II merged with the C45 aptamer (Stem II + C45) in the sensor 2_6, and of the corresponding region in the mutant 2_6m. Bases are colored according to reactivities shown in (A). The arrows demark the aptamer C45 (or its mutated version) within the C45-HHRz RNA device of 2_6 (or 2_6m), the sequences beyond the arrows belong to HHRz. C40U is a transition already observed in 2_6 at the level of high-throughput screening. See also Figure S8.

(Figure 6C) revealed a strand displacement that dramatically disrupts the folding of the merged stem II and the aptamer (Figures 7A and 7B). Thus, the structural elements identified *in vitro* to be critical for FBP binding by C45 aptamer are also essential for the FBP-dependent response of the sensor *in vivo*.

Finally, we wanted to get evidence that the FBP-dependent response of the sensor relies on its riboswitch activity. We hypothesized that, if FBP binding results in a conformational change of the RNA device, our sensor should occur *in vivo* as an equilibrium of two conformations: FBP free and FBP bound. To test if there are indeed two conformations of the sensor *in vivo*, we further analyzed DMS-MaPseq data. Compared with traditional DMS probing, DMS-MaPseq also has the advantage of recording multiple bases that were simultaneously single stranded as mutations within the same cDNA molecule (Homan et al., 2014; Morandi et al., 2021). By means of spectral clustering, this information can be exploited to identify multiple coexisting RNA conformations (Homan et al., 2014; Morandi et al., 2021). Here, spectral clustering analysis showed that the sensor 2_6 exists in two conformations within the cell (Figure S8, 2_6), likely corresponding to FBP-free and FBP-bound states. Consistent with the premise that these two conformations correspond to the FBP-free and -bound forms of the sensor, for the mutant 2_6m, which lacks FBP binding, we only observed one conformation *in vivo* (Figure S8, 2_6m). These results support the notion that an interaction of FBP with the sensor 2_6 triggers a conformational change necessary for the FBP-dependent response of the sensor.

## A developed FBP sensor functions as a glycolytic flux biosensor

Next, we wanted to apply our sensor to study metabolic heterogeneity. Since intracellular FBP concentrations were shown to correlate with the flux through glycolysis (Hackett et al., 2016; Kochanowski et al., 2013; Litsios et al., 2017), we hypothesized that our developed FBP sensor would be suitable for reporting glycolytic flux in single cells. Non-dividing cells, which can be present in normal yeast cultures, were shown to exhibit a reduced glucose uptake rate, and thus glycolytic flux, compared with the co-existing dividing cells (Litsios et al., 2019). To examine if the 2_6 FBP sensor can identify the different metabolic fluxes of dividing and non-dividing cells within the same yeast population, we cultured *TM6** cells with the sensor on glucose in a microfluidic device (Huberts et al., 2013; Lee et al., 2012) and monitored the GFP/mCherry ratio in both subpopulations. Here, we found a markedly higher GFP/mCherry ratio in the non-dividing cells compared with the dividing cells (Figure 8A), in line with the low glycolytic flux in the non-dividing cells. The same strain grown on maltose showed a ratio lower than that of cells dividing in glucose (Figure 8A), consistent with the higher FBP levels on this carbon source (Figure 3C), and the increased glycolytic flux. Across these three groups of cells, we could draw a notable correlation between the single-cell growth rate and the GFP/mCherry ratio (Figure 8A). In contrast, the *mutL* version of the sensor, which has impaired FBP binding (Figures 2C and 6C, mutant 2_6m), did not show any pronounced difference in the readout among the three groups of cells (Figure 8B).

To further test that our FBP sensor responds to changes in glycolytic flux dynamically, we perturbed the metabolism of WT cells with 2-deoxyglucose (2-DG), an inhibitor of glycolysis. Specifically, we monitored the readout of the sensor 2_6 in WT cells cultivated in the microfluidic device in the presence of glucose that were temporarily exposed to a sub-lethal dose of 2-DG. Here, observing that the drug decreased the cell division rate due to the reduction of the glycolytic flux, we found that the sensor's GFP/mCherry ratio significantly increased, which indicates, on average, a lower FBP level and glycolytic flux (Figure 8C). While the median ratios between the two populations were significantly different, the ratio distributions (i.e., with and without the inhibitor) partially overlapped, which could reflect not only the sensor-associated measurement error but also natural cell-to-cell differences in glycolytic flux among single cells. Remarkably, the glycolytic-flux-dependent modulation of the sensor's GFP/mCherry ratio proved to be reversible as the readout recovered to the original level when the 2-DG was removed from the medium (Figure 8C). Using the sensor's mutant 2_6m as a negative control, we did not find pronounced

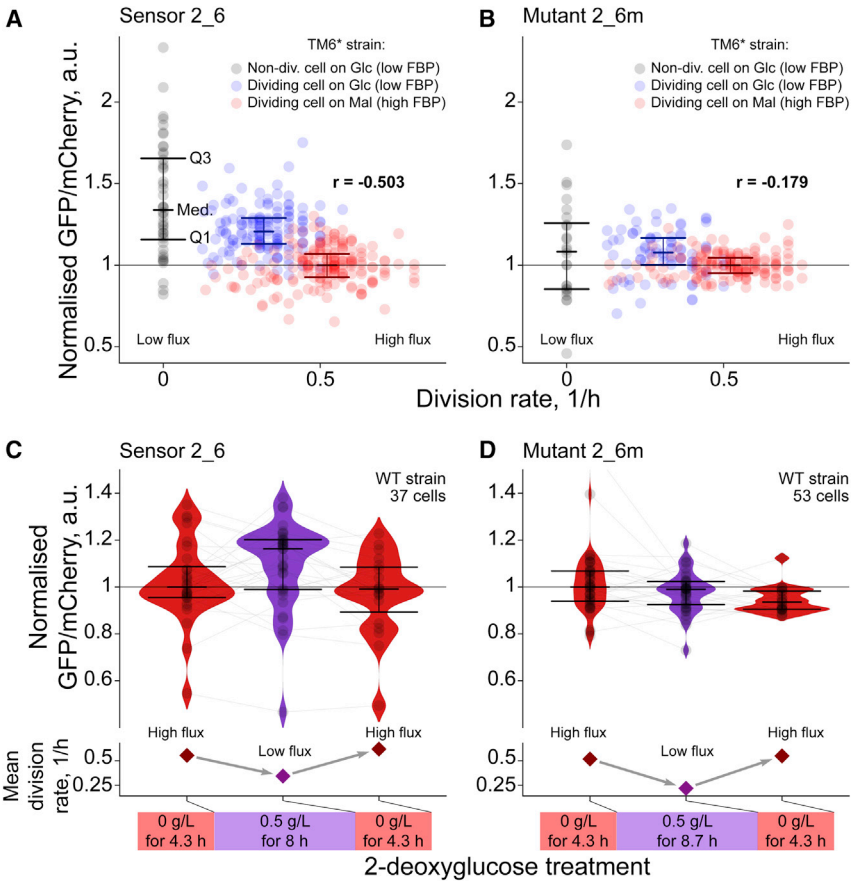


**Figure 8. The FBP sensor functions as a glycolytic flux biosensor**

(A and B) The GFP/mCherry ratio of the sensor 2_6 (A) or its mutant 2_6m (B) in three categories of cells: non-dividing TM6* cells consuming glucose (44 in 2_6 and 24 in 2_6m), dividing TM6* cells consuming glucose (138 in 2_6 and 77 in 2_6m), and dividing TM6* cells consuming maltose (183 in 2_6 and 151 in 2_6m). In the case of the dividing cells, a data unit is the mean GFP/mCherry ratio throughout one cell cycle (from budding to budding). For the category of the non-dividing cells, we calculate the mean GFP/mCherry ratio in a single-cell trajectory between 15 and 20 h after the last division. Q1, Q3, and Med. denote the lower and upper quartiles and the median. The sensor's and mutant's readouts are normalized by the respective median GFP/mCherry ratio values of dividing TM6* cells consuming maltose (horizontal line). The division rate is the reciprocal for the cell-cycle duration in the case of the dividing cells and zero in the case of the non-dividing cells. We assess the correlation using the Pearson's coefficient *r*.

(C and D) The GFP/mCherry ratio of the sensor 2_6 (C) or its mutant 2_6m (D) in single WT cells cultivated on 2% (20 g/L) glucose and dynamically exposed to 0.5 g/L 2-deoxyglucose for several hours. The black markers denote the single-cell GFP/mCherry ratio values averaged over 100 min before the indicated moments of the dynamic experiment. We present the readout of a cell after a particular phase of the treatment (indicated on the x axis) only if this cell was present in the microfluidic device during the whole phase. Cells present in the microfluidic device in multiple phases of the treatment are indicated with gray lines connecting black markers. Specifically, in both (C) and (D), 14 and 31 cells were present in three and two consecutive phases respectively, whereas the rest of the cells were present only during one full phase. The distributions of the readout are summarized via the violin plots as well as with the help of the lower and upper quartiles, and the median, as in (A). The sensor's and mutant's readouts are normalized by the respective median GFP/mCherry ratio values of the cells in the first phase of the treatment; that is, without the inhibitor (horizontal line). According to Mann-Whitney U test, in (C), the distributions significantly differ between the first and second phases (U = 338, n1 = 28, n2 = 35, p value = 0.036 two-sided) as well as between the second and third phases (U = 483, n1 = 35, n2 = 19, p value = 0.006 two-sided). In (D), the distributions do not differ between the first and second phases (U = 860, n1 = 41, n2 = 36, p value = 0.215 two-sided) and significantly differ between the second and third phases (U = 499, n1 = 36, n2 = 21, p value = 0.046 two-sided). The mean division rate is calculated as $\frac{N_b}{N_c \cdot \Delta t}$, where $N_c$ and $N_b$ are the total numbers of cells and buddings observed during the time $\Delta t$ hours of a particular phase of the treatment. Cellular-autofluorescence correction and smoothing of the single-cell traces are described in the STAR methods.

changes in the readout in response to 2-DG treatment (Figure 8D). Overall, these results demonstrate that the developed FBP sensor can distinguish cells with different glycolytic fluxes in clonal yeast cell populations, thus unveiling metabolic heterogeneity.

## DISCUSSION

In this work, we have developed an RNA-based sensor for the intracellular metabolite FBP, a glycolytic metabolite for which a natural riboswitch is not available. Specifically, we *in vitro* selected an RNA aptamer that selectively binds FBP—a doubly phosphorylated and non-aromatic compound—with millimolar affinity. Based on structural probing of this aptamer, we rationally designed a library of the aptamer-containing RNA devices that control GFP expression in yeast cells. Through FACS-seq, which combines cell sorting with NGS, we identified an RNA device that responds to changes in the physiological range of intracellular FBP levels. With DMS-MaPseq, a new method for *in vivo* structural probing, we demonstrated that *in vivo* FBP binding is essential for the functionality of the sensor. Because the intracellular FBP level correlates with the flux through glycolysis (Deutscher et al., 1995; Doan and Aymerich, 2003; Hackett et al., 2016; Huberts et al., 2012; Kochanowski et al., 2013; Litsios et al., 2017; Peeters et al., 2017; Zhang et al., 2017), our developed RNA-based sensor can be used as reporter for glycolytic flux in single cells.

An important element of our work was the selection of an aptamer that is suitable for FBP binding in living cells. While the quality of aptamers is traditionally judged on the basis of on their $K_D$ value (i.e., the lower, the better), here, we needed an aptamer with an affinity in the high micro- to low millimolar concentration range so that the physiological concentration changes of FBP could be transduced into differential sensor readouts. Still, the aptamer required high selectivity for FBP since many other phosphorylated sugars are simultaneously present in the cytosol, also

at micro- to millimolar concentrations (Canelas et al., 2011; Hackett et al., 2016). While the notion of a highly selective but low-affinity aptamer seems counterintuitive, interestingly, nature itself has evolved RNA-based regulatory systems that are selectively controlled by highly abundant metabolites (Ames and Breaker, 2011). For instance, the *glnA* riboswitch of cyanobacteria *Synechococcus elongatus* loosely binds L-glutamine in an open pocket; however, hydrogen bonds between the RNA and the heteroatoms of glutamine make the interaction highly specific (Ren et al., 2015). Similarly, since we found that neither fructose, fructose-1-phosphate, nor fructose-6-phosphate could compete with FBP for binding to the selected aptamer (Figures 1B and S2D), we conjecture that the two phosphate groups of FBP might play a crucial role in the observed selectivity.

Even after obtaining an *in vitro*-selected aptamer suitable for binding an intracellular metabolite within cells, there remains a grand challenge of coupling this aptamer with an actuator domain so that metabolite-induced conformational changes of the *in vitro*-selected aptamer can modulate the activity of the actuator domain *in vivo*. As our *in vitro*-selected aptamer folds as a stem-loop and alters its tertiary structure upon FBP binding (Figure 2B), we chose the HHRz as the actuator domain. Because the ribozyme's activity depends on tertiary-structure-stabilizing interactions between stem-loops I and II (Townshend et al., 2015), we reasoned that integration of the FBP aptamer into one of these stem-loops would modulate these interactions, and hence HHRz activity, by FBP binding. Thus, by considering the structural properties of our *in vitro*-selected aptamer, we increased the chance of obtaining a functional coupling between the sensing and actuator domains, and thereby generating a functional biosensor.

While high-throughput methods make it possible to screen large sensor libraries, the transformation efficiency of yeast is a severe bottleneck in conducting *in vivo* selection, as library sizes that can be screened are limited to around $10^5$ clones. In this work, we implemented measures to increase the effectiveness of screening for an RNA device that responds to FBP concentration *in vivo*. Specifically, we expanded the diversity of the RNA devices by generating six different libraries, where in each of them we fused the aptamer to the actuator's stem-loops in a different manner (Figure 3D). By doing so, we mitigated potential biases in the library design that could have resulted in unspecific alterations of HHRz activity. Moreover, we depleted RNA devices with a non-functional ribozyme from the input library, which allowed us to concentrate our screening capacity on variants that can potentially display FBP-dependent activity (Figures 3E and 3F). Despite the restricted search possibilities (as provided by the limited transformation efficiency of yeast), these measures allowed us to ultimately identify a sensor with FBP-dependent activity, suggesting that a combination of rational design and limited screening efforts here had an essential contribution to the successful development of the sensor.

To screen for an RNA device that responds to FBP concentration *in vivo*, it is necessary to be able to vary the intracellular ligand concentration. This requirement can be fulfilled in the development of sensors for xenobiotic compounds, because these compounds can exogenously be added to cell cultures at different concentrations, as done previously (Bayer and Smolke, 2005; Boussebayle et al., 2019; Groher et al., 2018; Jang et al., 2017; Porter et al., 2017; Suess et al., 2003; Weigand et al., 2008). However, modulation of the intracellular concentration of endogenous metabolites is highly challenging due to compensation by homeostatic mechanisms. In our screening, we exploited a combination of genetic and environmental perturbations in yeast that produced a 1-log concentration range of intracellular FBP concentration, corresponding to the physiological concentration changes of this metabolite. With this relatively narrow concentration range of FBP (in contrast to the xenobiotics), we nevertheless managed to develop a synthetic *in vivo*-functional RNA-based FBP sensor that displays a 50% overall change in the output signal. Moreover, the sensor is selective. We obtained the FBP aptamer in the presence of 0.3 M glucose, checked its selectivity *in vitro*, and performed both sensor validation and characterization along with a mutant that cannot bind FBP. While these measures provide evidence that the observed sensor output corresponds to changes in intracellular FBP levels, there is still no ultimate proof for it. Unfortunately, at the moment, it is not technically possible to generate such evidence.

Overall, with this work, we further pushed the RNA-based sensor development from the proof-of-concept stage to the demonstration that it is possible to develop—from scratch—RNA-based sensors for an endogenous metabolite for which there are no natural sensing RNA domains (i.e., riboswitches) available. In addition, as FBP reports the flux through glycolysis in organisms across kingdoms (Deutscher et al., 1995; Doan and Aymerich, 2003; Hackett et al., 2016; Huberts et al., 2012; Kochanowski et al., 2013; Litsios et al., 2017; Peeters et al., 2017; Zhang et al., 2017), the developed FBP sensor allows visualization of glycolytic flux in single cells. As the current sensor uses GFP expression to generate the signal output, it is most suitable for applications where cells are in steady state. Such applications can be found in research on metabolic heterogeneity, as well as in FACS-based screening approaches; e.g., to identify highly productive cell factories in a biotech context. Beyond, this sensor offers potential applications in synthetic biology, such as the engineering of genetic circuits where glycolytic flux serves as an input.

## SIGNIFICANCE

**Current RNA-based sensors for intracellular metabolites rely on natural metabolite-binding RNA elements from riboswitches. The limited availability of these natural RNA elements, however, restrains the development of novel intracellular metabolite sensors. While it is an established procedure to develop a metabolite-binding aptamer with SELEX, it is still challenging to convert this aptamer into a device that can be used inside cells to report the intracellular concentration of the metabolite. The challenge has to do with the difference between the *in vitro* selection conditions and the intracellular milieu, but also with the combinatorial complexity that emerges when the aptamer is combined with an actuator domain with the goal of relaying metabolite binding into a readable signal. This means that *in vivo* screening approaches are necessary. However, while it is currently possible to implement such screenings with small molecules that are not naturally produced and metabolized by the cell (i.e., xenobiotics), screening schemes with an endogenous metabolite as a ligand are far from trivial. Here, we have accomplished the development of an RNA-**

**based sensor for an intracellular metabolite, starting from the *in vitro* selection of a respective aptamer. Key for this was the combination of numerous techniques, including SELEX, aptamer characterization, *in vivo* screening with FACS-seq, a combination of genetic and environmental perturbations, as well as *in vivo* structural probing during validation. FBP, the actuating metabolite of the sensor, is a glycolytic intermediate whose concentration correlates with glycolytic activity in organisms across kingdoms. As such, our developed intracellular sensor for FBP can be used as a single-cell-based sensor for glycolytic flux.**

## STAR★METHODS

Detailed methods are provided in the online version of this paper and include the following:

- KEY RESOURCES TABLE
- RESOURCE AVAILABILITY
  - Lead contact
  - Materials availability
  - Data and code availability
- EXPERIMENTAL MODEL AND SUBJECT DETAILS
  - *S. cerevisiae* strains
  - Yeast cultivation
- METHOD DETAILS
  - *In vitro* selection of FBP aptamer
  - Binding assays with immobilized FBP
  - Preparation of metabolites
  - *In vitro* transcription
  - RNA labeling
  - Preparative denaturing urea-polyacrylamide gel electrophoresis
  - Binding assays with microscale thermophoresis
  - Selective 2'-hydroxyl acylation analyzed by primer extension
  - Quantification of intracellular concentration of fructose-1,6-bisphosphate
  - Determination of GFP/mCherry ratio by flow cytometry
  - Preparation of C45-HHRz library and HHRz versions for the *in vivo* reporter system
  - Sorting of cell subpopulations based on GFP/mCherry ratio by fluorescence-assisted cell sorting
  - Preparation of DNA library for NGS
  - Analysis of high-throughput *in vivo* screening (FACS-Seq) of RNA devices
  - Validation of FBP-sensor candidates
  - *In vivo* RNA structural mapping
  - Microscopy and image analysis
- QUANTIFICATION AND STATISTICAL ANALYSIS

## SUPPLEMENTAL INFORMATION

Supplemental information can be found online at https://doi.org/10.1016/j.chembiol.2021.04.006.

## ACKNOWLEDGMENTS

The research leading to these results has received funding (M.H.) from the European Union Seventh Framework Programme (FP7-KBBE-2013-7-single-stage) under grant agreement no. 613745 (PROMYS), from the European Union Seventh Framework Programme under grant agreement no. 289995 (ISOLATE), and from the European Union Horizon 2020 Programme under grant agreement no. 642738, (MetaRNA). The authors would like to thank Prof. Arnold Driessen for kindly sharing the Monolith for MST analyses, Prof. Christina Smolke and Dr. Brent Townshend for plasmids to implement the *in vivo* reporter system and useful discussions, Dr. Alicia Barroso for capillary electrophoresis analysis of SHAPE samples, Dr. Athanasios Litsios for initial single-cell microscopy analyses and critical discussions, and Dr. Andreas Milias-Argeitis, Prof. Antonio Murciano, Dr. Jakub Radzikowski, and Dr. Joana Saldida for input on data analysis.

## AUTHOR CONTRIBUTIONS

Y.L. selected the aptamer and performed binding experiments with immobilized FBP mentored by F.E. and supervised by L.F.O. and G.M. A.D.O. performed and analyzed binding experiments by microscale thermophoresis. N.M.-F. performed and analyzed SHAPE experiments. S.R.V. quantified intracellular FBP. A.D.O. and S.R.V. characterized the *in vivo* reporter system, prepared C45-HHRz libraries in *E. coli* and yeast, and performed the pre-selection and sorting of yeast libraries. A.D.O. prepared DNA library for NGS. V.T. designed and implemented the data analysis for the high-throughput screening with a conceptual contribution from A.D.O. A.D.O., S.R.V., and V.T. validated sensor candidates. V.T. investigated the sensor's dynamic range across multiple strains. D.I. implemented and analyzed *in vivo* RNA structural probing. V.T. performed and analyzed microscopy experiments. M.H. conceived the project and secured funding for it. A.D.O. designed and directed the overall course of the study. A.D.O., V.T., and M.H. wrote the manuscript.

## DECLARATION OF INTERESTS

The authors declare no competing interests.

Received: December 21, 2020
Revised: February 25, 2021
Accepted: April 6, 2021
Published: April 28, 2021

## REFERENCES

Ames, T.D., and Breaker, R.R. (2011). Bacterial aptamers that selectively bind glutamine. RNA Biol. *8*, 82–89.

Bayer, T.S., and Smolke, C.D. (2005). Programmable ligand-controlled riboregulators of eukaryotic gene expression. Nat. Biotechnol. *23*, 337–343.

Bley Folly, B., Ortega, A.D., Hubmann, G., Bonsing-Vedelaar, S., Wijma, H.J., van der Meulen, P., Milias-Argeitis, A., and Heinemann, M. (2018). Assessment of the interaction between the flux-signaling metabolite fructose-1,6-bisphosphate and the bacterial transcription factors CggR and Cra. Mol. Microbiol. *109*, 278–290.

Bose, D., Su, Y., Marcus, A., Raulet, D.H., and Hammond, M.C. (2016). An RNA-based fluorescent biosensor for high-throughput analysis of the cGAS-cGAMP-STING pathway. Cell Chem. Biol. *23*, 1539–1549.

Boussebayle, A., Torka, D., Ollivaud, S., Braun, J., Bofill-Bosch, C., Dombrowski, M., Groher, F., Hamacher, K., and Suess, B. (2019). Next-level riboswitch development—implementation of Capture-SELEX facilitates identification of a new synthetic riboswitch. Nucleic Acids Res. *47*, 4883–4895.

Canelas, A.B., Ras, C., ten Pierick, A., van Gulik, W.M., and Heijnen, J.J. (2011). An in vivo data-driven framework for classification and quantification of enzyme kinetics and determination of apparent thermodynamic data. Metab. Eng. *13*, 294–306.

Delvigne, F., Zune, Q., Lara, A.R., Al-Soud, W., and Sørensen, S.J. (2014). Metabolic variability in bioprocessing: Implications of microbial phenotypic heterogeneity. Trends Biotechnol. *32*, 608–616.

Deutscher, J., Küster, E., Bergstedt, U., Charrier, V., and Hillen, W. (1995). Protein kinase-dependent HPr/CcpA interaction links glycolytic activity to carbon catabolite repression in Gram-positive bacteria. Mol. Microbiol. *15*, 1049–1053.

Doan, T., and Aymerich, S. (2003). Regulation of the central glycolytic genes in *Bacillus subtilis*: binding of the repressor CggR to its single DNA target sequence is modulated by fructose-1,6-bisphosphate. Mol. Microbiol. *47*, 1709–1721.

Elbing, K., Larsson, C., Bill, R.M., Albers, E., Snoep, J.L., Boles, E., Hohmann, S., and Gustafsson, L. (2004a). Role of hexose transport in control of glycolytic flux in *Saccharomyces cerevisiae*. Appl. Environ. Microbiol. *70*, 5323–5330.

Elbing, K., Ståhlberg, A., Hohmann, S., and Gustafsson, L. (2004b). Transcriptional responses to glucose at different glycolytic rates in *Saccharomyces cerevisiae*. Eur. J. Biochem. *271*, 4855–4864.

Van Eunen, K., Bouwman, J., Daran-Lapujade, P., Postmus, J., Canelas, A.B., Mensonides, F.I.C., Orij, R., Tuzun, I., Van Den Brink, J., Smits, G.J., et al. (2010). Measuring enzyme activities under standardized in vivo-like conditions for systems biology. FEBS J. *277*, 749–760.

Ferrezuelo, F., Colomina, N., Palmisano, A., Garí, E., Gallego, C., Csikász-Nagy, A., and Aldea, M. (2012). The critical size is set at a single-cell level by growth rate to attain homeostasis and adaptation. Nat. Commun. *3*, 1012.

Gao, X., Dong, X., Subramanian, S., Matthews, P.M., Cooper, C.A., Kearns, D.B., and Dann, C.E. (2014). Engineering of *Bacillus subtilis* strains to allow rapid characterization of heterologous diguanylate cyclases and phosphodiesterases. Appl. Environ. Microbiol. *80*, 6167–6174.

Gietz, R.D., and Schiestl, R.H. (2007). Large-scale high-efficiency yeast transformation using the LiAc/SS carrier DNA/PEG method. Nat. Protoc. *2*, 38–41.

Groher, F., Bofill-bosch, C., Schneider, C., Braun, J., Jager, S., Geißler, K., Hamacher, K., and Suess, B. (2018). Riboswitching with ciprofloxacin — development and characterization of a novel RNA regulator. Nucleic Acids Res. *46*, 2121–2132.

Hackett, S.R., Zanotelli, V.R.T., Xu, W., Goya, J., Park, J.O., Perlman, D.H., Gibney, P.A., Botstein, D., Storey, J.D., and Rabinowitz, J.D. (2016). Systems-level analysis of mechanisms regulating yeast metabolic flux. Science *354*, aaf2786.

Homan, P.J., Favorov, O.V., Lavender, C.A., Kursun, O., Ge, X., Busan, S., Dokholyan, N.V., and Weeks, K.M. (2014). Single-molecule correlated chemical probing of RNA. Proc. Natl. Acad. Sci. U S A *111*, 13858–13863.

Huberts, D.H.E.W., Niebel, B., and Heinemann, M. (2012). A flux-sensing mechanism could regulate the switch between respiration and fermentation. FEMS Yeast Res. *12*, 118–128.

Huberts, D.H.E.W., Sik Lee, S., Gonzáles, J., Janssens, G.E., Vizcarra, I.A., and Heinemann, M. (2013). Construction and use of a microfluidic dissection platform for long-term imaging of cellular processes in budding yeast. Nat. Protoc. *8*, 1019–1027.

Incarnato, D., Morandi, E., Simon, L.M., and Oliviero, S. (2018). RNA framework: an all-in-one toolkit for the analysis of RNA structures and post-transcriptional modifications. Nucleic Acids Res. *46*, e97.

Inoue, H., Nojima, H., and Okayama, H. (1990). High efficiency transformation of Escherichia coli with plasmids. Gene *96*, 23–28.

Jang, S., Jang, S., Xiu, Y., Kang, T.J., Lee, S.H., Koffas, M.A.G., and Jung, G.Y. (2017). Development of artificial riboswitches for monitoring of naringenin in vivo. ACS Synth. Biol. *6*, 2077–2085.

Johnson, C.H., Ivanisevic, J., and Siuzdak, G. (2016). Metabolomics: beyond biomarkers and towards mechanisms. Nat. Rev. Mol. Cell Biol. *17*, 451–459.

Karabiber, F., McGinnis, J.L., Favorov, O.V., and Weeks, K.M. (2013). QuShape: rapid, accurate, and best-practices quantification of nucleic acid probing information, resolved by capillary electrophoresis. RNA *19*, 63–73.

Kellenberger, C.A., Wilson, S.C., Sales-Lee, J., and Hammond, M.C. (2013). RNA-based fluorescent biosensors for live cell imaging of second messengers cyclic di-GMP and cyclic AMP-GMP. J. Am. Chem. Soc. *135*, 4906–4909.

Kellenberger, C.A., Chen, C., Whiteley, A.T., Portnoy, D.A., and Hammond, M.C. (2015). RNA-based fluorescent biosensors for live cell imaging of second messenger cyclic di-AMP. J. Am. Chem. Soc. *137*, 6432–6435.

Kim, J., and DeBerardinis, R.J. (2019). Mechanisms and implications of metabolic heterogeneity in cancer. Cell Metab. *30*, 434–446.

Kochanowski, K., Volkmer, B., Gerosa, L., Haverkorn van Rijsewijk, B.R., Schmidt, A., and Heinemann, M. (2013). Functioning of a metabolic flux sensor in *Escherichia coli*. Proc. Natl. Acad. Sci. U S A *110*, 1130–1135.

Langmead, B., and Salzberg, S.L. (2012). Fast gapped-read alignment with Bowtie 2. Nat. Methods *9*, 357–359.

Lee, S.W., and Oh, M.K. (2015). A synthetic suicide riboswitch for the high-throughput screening of metabolite production in *Saccharomyces cerevisiae*. Metab. Eng. *28*, 143–150.

Lee, S.S., Avalos Vizcarra, I., Huberts, D.H.E.W., Lee, L.P., and Heinemann, M. (2012). Whole lifespan microscopic observation of budding yeast aging through a microfluidic dissection platform. Proc. Natl. Acad. Sci. U S A *109*, 4916–4920.

Liang, J.C., Chang, A.L., Kennedy, A.B., and Smolke, C.D. (2012). A high-throughput, quantitative cell-based screen for efficient tailoring of RNA device activity. Nucleic Acids Res. *40*, e154.

Litsios, A., Ortega, A.D., Wit, E.C., and Heinemann, M. (2017). Metabolic-flux dependent regulation of microbial physiology. Curr. Opin. Microbiol. *42*, 71–78.

Litsios, A., Huberts, D.H.E.W., Terpstra, H.M., Guerra, P., Schmidt, A., Buczak, K., Papagiannakis, A., Rovetta, M., Hekelaar, J., Hubmann, G., et al. (2019). Differential scaling between G1 protein production and cell size dynamics promotes commitment to the cell division cycle in budding yeast. Nat. Cell Biol. *21*, 1382–1392.

Long, Y., Pfeiffer, F., Mayer, G., Schrøder, T.D., Özalp, V.C., and Olsen, L.F. (2016). Selection of aptamers for metabolite sensing and construction of optical nanosensors. Methods Mol. Biol. *1380*, 3–19.

McGinnis, J.L., Duncan, C.D.S., and Weeks, K.M. (2009). High-throughput SHAPE and Hydroxyl Radical Analysis of RNA Structure and Ribonucleoprotein Assembly. Methods Enzymol.*468* (Elsevier Inc.), pp. 67–89.

Monteiro, F., Hubmann, G., Takhaveev, V., Vedelaar, S.R., Norder, J., Hekelaar, J., Saldida, J., Litsios, A., Wijma, H.J., Schmidt, A., et al. (2019). Measuring glycolytic flux in single yeast cells with an orthogonal synthetic biosensor. Mol. Syst. Biol. *15*, 1–20.

Morandi, E., Manfredonia, I., Simon, L.M., Anselmi, F., van Hemert, M.J., Oliviero, S., and Incarnato, D. (2021). Genome-scale deconvolution of RNA structure ensembles. Nat. Methods *18*, 249–252.

Ozalp, V.C., Pedersen, T.R., Nielsen, L.J., and Olsen, L.F. (2010). Time-resolved measurements of intracellular ATP in the yeast *Saccharomyces cerevisiae* using a new type of nanobiosensor. J. Biol. Chem. *285*, 37579–37588.

Paige, J.S., Nguyen-Duc, T., Song, W., and Jaffrey, S.R. (2012). Fluorescence imaging of cellular metabolites with RNA. Science *335*, 1194.

Peeters, K., Van Leemputte, F., Fischer, B., Bonini, B.M., Quezada, H., Tsytlonok, M., Haesen, D., Vanthienen, W., Bernardes, N., Gonzalez-Blas, C.B., et al. (2017). Fructose-1,6-bisphosphate couples glycolytic flux to activation of Ras. Nat. Commun. *8*, 922.

Porter, E.B., Polaski, J.T., Morck, M.M., and Batey, R.T. (2017). Recurrent RNA motifs as scaffolds for genetically encodable small-molecule biosensors. Nat. Chem. Biol. *13*, 295–301.

Radzikowski, J.L., Vedelaar, S., Siegel, D., Ortega, Á.D., Schmidt, A., and Heinemann, M. (2016). Bacterial persistence is an active σS stress response to metabolic flux limitation. Mol. Syst. Biol. *12*, 882.

Reetz, M.T., Kahakeaw, D., and Lohmer, R. (2008). Addressing the numbers problem in directed evolution. Chembiochem *9*, 1797–1804.

Ren, A., Xue, Y., Peselis, A., Serganov, A., Al-Hashimi, H.M., and Patel, D.J. (2015). Structural and dynamic basis for low-affinity, high-selectivity binding of L-glutamine by the glutamine riboswitch. Cell Rep. *13*, 1800–1813.

Reuter, J.S., Mathews, D.H., Miranti, C.K., Beck, A., Polyak, K., Toker, A., Sethi, T., Bourget, L., Lamoureux, L., and Lo, R. (2010). RNAstructure: software for RNA secondary structure prediction and analysis. BMC Bioinformatics *11*, 129.

Rugbjerg, P., and Sommer, M.O.A. (2019). Overcoming genetic heterogeneity in industrial fermentations. Nat. Biotechnol. *37*, 869–876.

Schindelin, J., Arganda-Carrera, I., Frise, E., Verena, K., Mark, L., Tobias, P., Stephan, P., Curtis, R., Stephan, S., Benjamin, S., et al. (2009). Fiji - an Open platform for biological image analysis. Nat. Methods *9*, 241.

Schmidt, A.M. (2014). Flux-signaling and flux-dependent regulation in *Saccharomyces cerevisae* (ETH Zurich).

Schreiber, F., and Ackermann, M. (2020). Environmental drivers of metabolic heterogeneity in clonal microbial populations. Curr. Opin. Biotechnol. *62*, 202–211.

Su, Y., Hickey, S.F., Keyser, S.G.L., and Hammond, M.C. (2016). In vitro and in vivo enzyme activity screening via RNA-based fluorescent biosensors for S-Adenosyl- l -homocysteine (SAH). J. Am. Chem. Soc. *138*, 7040–7047.

Suess, B., Hanson, S., Berens, C., Fink, B., Schroeder, R., and Hillen, W. (2003). Conditional gene expression by controlling translation with tetracycline-binding aptamers. Nucleic Acids Res. *31*, 1853–1858.

Takhaveev, V., and Heinemann, M. (2018). Metabolic heterogeneity in clonal microbial populations. Curr. Opin. Microbiol. *45*, 30–38.

Tasdogan, A., Faubert, B., Ramesh, V., Ubellacker, J.M., Shen, B., Solmonson, A., Murphy, M.M., Gu, Z., Gu, W., Martin, M., et al. (2020). Metabolic heterogeneity confers differences in melanoma metastatic potential. Nature *577*, 115–120.

Townshend, B., Kennedy, A.B., Xiang, J.S., and Smolke, C.D. (2015). High-throughput cellular RNA device engineering. Nat. Methods *12*, 989–994.

Verduyn, C., Postma, E., Scheffers, W.A., and Van Dijken, J.P. (1992). Effect of benzoic acid on metabolic fluxes in yeasts: a continuous-culture study on the regulation of respiration and alcoholic fermentation. Yeast *8*, 501–517.

van der Walt, S., Schönberger, J.L., Nunez-Iglesias, J., Boulogne, F., Warner, J.D., Yager, N., Gouillart, E., and Yu, T. (2014). scikit-image: image processing in Python. PeerJ *2*, e453.

Weigand, J.E., Sanchez, M., Gunnesch, E., Zeiher, S., Schroeder, R., and Suess, B. (2008). Screening for engineered neomycin riboswitches that control translation initiation. RNA, 89–97.

Wilkinson, K.A., Merino, E.J., and Weeks, K.M. (2006). Selective 2'-hydroxyl acylation analyzed by primer extension (SHAPE): quantitative RNA structure analysis at single nucleotide resolution. Nat. Protoc. *1*, 1610–1616.

Yang, J., Seo, S.W., Jang, S., Shin, S.-I.I., Lim, C.H., Roh, T.-Y.Y., and Jung, G.Y. (2013). Synthetic RNA devices to expedite the evolution of metabolite-producing microbes. Nat. Commun. *4*, 1413.

You, M., Litke, J.L., and Jaffrey, S.R. (2015). Imaging metabolite dynamics in living cells using a Spinach-based riboswitch. Proc. Natl. Acad. Sci. U S A *112*, E2756–E2765.

Zhang, A., Cheng, T.P.O., Wu, X.Y., Altura, B.T., and Altura, B.M. (1997). Extracellular $Mg^{2+}$ regulates intracellular $Mg^{2+}$ and its subcellular compartmentation in fission yeast, *Schizosaccharomyces pombe*. Cell. Mol. Life Sci. *53*, 69–72.

Zhang, C.-S., Hawley, S.A., Zong, Y., Li, M., Wang, Z., Gray, A., Ma, T., Cui, J., Feng, J.-W., Zhu, M., et al. (2017). Fructose-1,6-bisphosphate and aldolase mediate glucose sensing by AMPK. Nature *548*, 112–116.

Zubradt, M., Gupta, P., Persad, S., Lambowitz, A.M., Weissman, J.S., and Rouskin, S. (2017). DMS-MaPseq for genome-wide or targeted RNA structure probing in vivo. Nat. Methods *14*, 75–82.

## STAR★METHODS

### KEY RESOURCES TABLE

| REAGENT or RESOURCE | SOURCE | IDENTIFIER |
|---|---|---|
| Chemicals, peptides, and recombinant proteins | | |
| D-fructose-1,6-bisphosphate | Sigma | F6803 |
| T7 RNA polymerase | Laboratory of Beatrix Suess | N/A |
| 1-methyl-6-nitroisatoic anhydride | Sigma | S888079 |
| Dimethyl sulfate (DMS) | Sigma | D186309 |
| Critical commercial assays | | |
| TGIRT-III | InGex | TGIRT50 |
| NEBNext Ultra II DNA Library Prep Kit | New England Biolabs | E7645S |
| Gibson Assembly mix | New England Biolabs | E2611 |
| Q5® High-Fidelity DNA Polymerase | New England Biolabs | M0515 |
| Experimental models: organisms/strains | | |
| KOY wild type, ura3-52 | (Elbing et al., 2004a, 2004b) | KOY.PK2-1C82 |
| KOY-VW100 TM6*, ura3-52 | (Elbing et al., 2004a, 2004b) | KOY.TM6* |
| Oligonucleotides | | |
| Primers used in this study. Table S5. | This paper | N/A |
| Recombinant DNA | | |
| pCS1748 plasmid | Laboratory of Christina Smolke | pCS1748 |
| pFBP-2_6.sensor plasmid | This paper | Addgene plasmid #162800 |
| pFBP-2_6m.mutant plasmid | This paper | Addgene plasmid #162842 |
| FBP aptamer C45: GGGAGGACGAUGCGGUUCCUCAU GUGUUGACGACUCGCUGAGGAUCCGAGA | This paper | N/A |
| Sensor 2_6 (RNA device): GCTGTCACCGGAATAGGAG TCCGGTCTGATGAGTCCACTTGCTGAGGATCCGACG GTTCCTCATGTGTTGACGAAGGACGAAACAGC | This paper | N/A |
| Mutant 2_6m (RNA device): GCTGTCACCGGAATAGGA GTCCGGTCTGATGAGTCCTGTTGCTGAGGATCCGAC GGTTCCTCATGTGAACTGCTTGGACGAAACAGC | This paper | N/A |
| Software and algorithms | | |
| Fiji-ImageJ | (Schindelin et al., 2009) | https://imagej.net/Fiji |
| Python version 3.6.2 | Python Software Foundation | https://www.python.org/ |
| Kaluza Analysis Software | Beckman Coulter | N/A |
| BudJ | (Ferrezuelo et al., 2012) | N/A |
| GraphPad Prism 5.0 | GraphPad Software | https://www.graphpad.com/ |
| RNA structure | (Reuter et al., 2010) | http://rna.urmc.rochester.edu/RNAstructure.html |
| QuShape | (Karabiber et al., 2013) | https://weekslab.com/software/qushape/ |
| Other | | |
| Monolith NT.115 Green Red MST | Nanotemper technologies | N/A |
| Microfluidic device | Laboratory of Matthias Heinemann | N/A |
| MoFlo Astrios (cell sorter) | Beckman Coulter | N/A |
| Accuri™ C6 (flow cytometer) | Becton Dickinson | N/A |
| CFX Connect™ Real-Time PCR Detection System | Bio-Rad | N/A |

## RESOURCE AVAILABILITY

### Lead contact

Further information and requests for resources and reagents should be directed to and will be fulfilled by the lead contact, Matthias Heinemann, m.heinemann@rug.nl.

### Materials availability

Strains are available from the corresponding author on reasonable request. Plasmids are available from Addgene (plasmids #162800, #162842, #162844, #162869).

### Data and code availability

The datasets generated during and/or analyzed during the current study are available from the corresponding author on reasonable request. Computer code used to analyze the data are available from the corresponding author on reasonable request.

## EXPERIMENTAL MODEL AND SUBJECT DETAILS

### *S. cerevisiae* strains

KOY wild type (WT), KOY-VW100 *HXT7* (*HXT7*), KOY-VW100 *TM3* (*TM3*), KOY-VW100 *TM4* (*TM4*) and KOY-VW100 *TM6** (*TM6**) (Elbing et al., 2004b), all with *ura3-52* auxotrophy, plus WT and *TM6** without *ura3-52* auxotrophy for microscopic analyses.

### Yeast cultivation

Unless specifically indicated, yeast were cultivated in 500 mL-flasks containing 50 mL of Verduyn's minimal medium (Verduyn et al., 1992) buffered at pH 5 with 10 mM KH-phthalate, and inoculated with exponentially growing cells. Starting cell density (0.75-2.0x $10^6$ cells $mL^{-1}$) was adjusted to the foreseen time of cultivation and each strain's growth rate so that the culture never achieved densities higher than 2.5-3.0x $10^7$ cells $mL^{-1}$. To obtain a homogeneous culture of cells adapted to the carbon source and with a metabolic steady state, cells were allowed to grow at least for 20 generations through two pre-culturing steps prior to the main culture. The inoculum was prepared in the identical minimal medium. All cultivations were performed at 30 ℃, and cultures were continuously shaken at 300 rpm. To make competent cells, we used Yeast Peptone broth (20 $gL^{-1}$ peptone, 10 g $L^{-1}$ yeast extract). To recover cells after sorting, we used Yeast Nitrogen Base (YNB) supplemented with Complete Supplement Mixture (CSM) dropout without uracil and 400 μg $mL^{-1}$ of G418. All nutrients and supplements to make media were purchased to Foremedium™ (London, UK). All culture media were supplemented with either 20 g $L^{-1}$ of D-glucose or maltose (both from Merck Millipore).

For microfluidic cultivation, several days before a microscopy experiment, we recovered necessary strains from their glycerol stocks stored at -80°C, by growing them for two days on 2%-glucose agar plates. For each strain, a single colony was inoculated in 10 mL of Verduyn's minimal medium in a 100-mL Erlenmeyer flask, which initiated a pre-culture that was cultivated overnight at 30°C with shaking at the speed of 300 rpm. Cells still growing exponentially in the pre-culture were diluted at the $OD_{600}$=0.025-0.05 in the fresh medium and cultivated for several hours under the same conditions until the $OD_{600}$=0.1-0.2. Afterwards, cells were loaded in the microfluidic device as described previously(Huberts et al., 2013; Lee et al., 2012). In the microfluidic device, cells were constantly provided with the fresh medium at the flow rate of 4-5 μL/min via a syringe pump (for Figures 8A, 8B, and 8D) or an air-pressurized pumping system (OB1, Elveflow) assisted by a flow sensor (MFS2, Elveflow) (for Figure 8C). During cultivation in the microfluidic device, the temperature was maintained at 30°C with the help of a microscope incubator. Cell cultivation in the two consecutive flask cultures and the microfluidic device was done on the same carbon source, namely, 2% (20 g/L) glucose or 2% maltose. For Figures 8A and 8B, we cultivated different strains simultaneously in two microfluidic devices attached to one cover glass: in one device, we loaded *TM6** cells with the sensor 2_6, and *TM6** cells without fluorescent proteins and *ura3-52* auxotrophy (for further cell-autofluorescence correction); in the other device, we loaded *TM6** cells with the mutant 2_6m, and also *TM6** cells without fluorescent proteins and *ura3-52* auxotrophy. For Figures 8C and 8D, we cultivated WT cells with the sensor 2_6 and the mutant 2_6m in microfluidic devices on different days. In both cases, we also loaded into the microfluidic device WT cells without fluorescent proteins and *ura3-52* auxotrophy for further cell autofluorescence correction.

For *in vivo* RNA structural mapping, *TM6** cells with the sensor 2_6 and the mutant 2_6m were cultivated in two consecutive exponential cultures in 10 mL of Verduyn's minimal medium with 2% glucose and 2% maltose in 100-mL Erlenmeyer flasks.

## METHOD DETAILS

### *In vitro* selection of FBP aptamer

C45 was selected from an RNA pool (5'-GGGAGGACGAUGCGG-N40-CAGACGACUCGCUGAGGAUCCGAGA-3', where N40 represents a 40 nucleotide-long variable region) according to a previously described method (Long et al., 2016). In brief, 100 μL of D-fructose-1,6-bisphosphate (FBP) immobilized to epoxy-activated sepharose by 1,4-butanediol-diglycidyl-ether equilibrated with cytosolic buffer *CB* (6 mM $KH_2PO_4$, 14 mM $K_2HPO_4$, 140 mM KCl, 10 mM NaCl, 5 mM $MgCl_2$, 5.5% glucose, pH 6.8) was mixed with 1 nmol of the RNA pool in a final volume of 400 μL and let to settle by gravity at 25ºC. In rounds 1 to 3, prior to the incubation with FBP-sepharose, the RNA pool was pre-cleared with the same volume of sepharose. After incubation, the column was washed twice

with 600 μL of CB and the RNA bound eluted. Elution buffer was 5 mM EDTA in rounds 1 to 3, and 5mM FBP in CB in rounds 4 to 13. RNA was precipitated from the eluates with 30 mM sodium acetate in ethanolic solution and 10 μg of glycogen, retrotranscribed with Superscript II (Invitrogen; Carlsbad, CA) at 54ºC for 10 min and the resulting cDNA amplified with GoTaq Flexi DNA polymerase (Promega; Madison, WI) for 8 PCR cycles in the same reaction with a final volume of 100 μL. 10 μL of the amplification product was used as template to synthesize the RNA pool for the next round by *in vitro* transcription with T7 RNA polymerase at 37ºC for 20 minutes. RT-PCR products obtained from round 13 were cloned with TOPO TA Kit (Invitrogen; Carlsbad, CA) according to the manufacturer's indications, and plasmids extracted from individual bacterial clones sent for Sanger sequencing using the T3 primer.

### Binding assays with immobilized FBP

CAL Fluor Red 610-labelled RNA sequences were purchased from LGC Biosearch Technologies (Risskov, Denmark). 560 μl of FBP-sepharose were mixed with 8.4 mL of 20 nM CAL Fluor Red 610-labelled RNAs in a Econo-Column Chromatography Column (BioRad, Hercules,CA), and the column washed with CB until no fluorescence change was detected in the flow-through. The resin was then resuspended in 8.4 mL of CB and evenly distributed among seven empty polypropylene spin columns, from which the RNA was eluted using different concentrations of FBP (1.2 mL; 0.03, 0.13, 0.50, 2.0, 8.0, 32, 128 mM). The percentage of eluted RNA was calculated by measuring the fluorescence intensity in the eluted fractions and the one remaining in their respective columns with an Edinburgh FS920 spectrofluorometer (Edinburgh Instruments, Edinburgh, U.K.) using an excitation wavelength of 590 nm (slit of 5 nm) and an emission of 615 nm (slit of 20 nm) in a final volume of 1.2 mL for all samples in a 10mm x 10mm quartz cuvette. Specificity assays were performed as described but using 200 μl of FBP-sepharose and 1.2 mL of 20 nM CAL Fluor Red 610-labelled RNA and eluted with 1.2 mL 10 mM of glucose-6-phosphate, fructose-6-phosphate, adenosine-triphosphate and FBP (all from Sigma; St. Louis, MO). All measurements were performed in triplicate. Data were analyzed using GraphPad Prism 5.0, where a non-linear regression (assumptions: one binding-site – specific binding) with the least squares fitting method was used to model binding behavior and the $K_D$.

### Preparation of metabolites

To remove the $Na^+$ present in commercially-available salts of phosphorylated metabolites (fructose-1-phosphate, fructose-1,6-bisphosphate) these compounds were dialyzed prior to binding analyses. The compounds were dissolved in 2x CB, and mQ $H_2O$ was then added to reach a final concentration around 1.5M in 1x CB. This stock solution was dialyzed in a Spectrum Micro Float-A-Lyzer with a MW cut-off 0.1-0.5 kDa (Thermo Fisher Sci.; Waltham, MA) against 1L of CB with additional 2M glucose to prevent osmosis. Dialysis was let to proceed for 24 hours with continuous stirring at 4ºC including two changes of the outer buffer. After dialysis, the pH of FBP solution was checked and adjusted to 7.0 if necessary, and the concentration determined by HPLC. In brief, a series of dilutions of the dialyzed stock were run through a HiPLEX column (Agilent, Santa Clara, CA) for 20 minutes in 0.005 M $H_2SO_4$. A unique peak at 6.4 min was integrated and the values interpolated in a standard curve run alongside.

### *In vitro* transcription

DNA templates for *in vitro* transcription of RNA aptamers were generated by hybridization two complementary single stranded DNA oligonucleotides (ADO-01 to ADO-12; Table S5). 150 μL of each oligo at 200 μM in TE buffer (10 mM Tris-HCl, 1 mM EDTA, pH = 8) were mixed, and the mix heated at 95ºC for 5 minutes and then cooled down to 70ºC with a -1ºC/min slope. Hybridization was monitored by poly-acrylamide gel electrophoresis (PAGE) in a 6% PA - 1x TBE (89 mM Tris, 89 mM boric acid, 2 mM EDTA) gel using 0.5x TBE as running buffer for 20 min at 300V. The gel was stained with a 1:10,000 solution of Invitrogen SYBR safe (Thermo Fisher Sci.; Waltham, MA) in 1x TBE for 5 min and visualized in a UV transilluminator.

0.1 μM of template DNA was transcribed *in vitro* for 4 hours at 37ºC with 1 U/μl T7 polymerase. His-tagged T7 RNA polymerase (kindly provided by Beatrix Suess, TU Darmstadt) was expressed in *E. coli* and purified with $Ni^{2+}$-sepharose column. The transcription mix also included, 1x transcription buffer, NTPs 2.5 mM each, 0.2 U/μL RNase inhibitor, 0.1 mU/μL inorganic pyrophosphatase (all from Thermo Fisher Sci.; Waltham, MA), 2 mM spermidine (Sigma, St. Louis, MO) in a final volume of 0.3 mL. To generate 5'-thio-modified RNA for RNA labeling, the reaction mix also included 10 mM guanosine-5'-thiophosphate (GMPS; Genaxxon bioscience, Ulm, Germany). Nucleic acids were precipitated with 0.3 M sodium acetate in ethanolic solution, and then template DNA digested using Turbo DNA-free kit (Thermo Fisher Sci.) for 1h at 37ºC following manufacturer's instructions. DNA-free RNA was precipitated with sodium acetate, and purified by preparative denaturing urea-PAGE. RNA pellets from 5'-thio-modified RNA transcription were re-dissolved in coupling buffer (8M urea, 2 mM Tris-HCl, 20 mM EDTA pH = 7.0), and DTT was then added to a final concentration of 60 mM. After a 1 hour-incubation, un-incorporated GMPS and DTT were removed by gel filtration using two Zeba Spin desalting columns (Thermo Fisher Sci.) sequentially.

### RNA labeling

50 nmol of Cy5-maleimide (GE Healthcare, Chicago, IL) dissolved in anhydrous DMSO (Thermo Fisher) were mixed with 150 nmol of RNA (from 5'-thio-modification procedure) in coupling buffer and incubated for 2 h at 37ºC in the dark. Cy5-labeled RNA was purified by preparative denaturing urea-PAGE. The integrity and purity of labeled RNA was monitored by denaturing PAGE, being the gels stained with SYBR safe and scanned with a Typhoon 9410 (two channels: 488/520 for SYBR; and 640/674 nm for Cy5) and analyzed with ImageQuant TL1 Software (GE Healthcare). Cy5-RNA concentration was determined in a Spark 10M multimode reader using a nanoquant plate (Tecan, Männedorf, Switzerland).

### Preparative denaturing urea-polyacrylamide gel electrophoresis

DNA-free RNA from *in vitro* transcription and Cy5-labeled RNA from coupling reactions precipitated with sodium acetate were re-dissolved in Bartel/Lau loading buffer (8M urea, 2 mM Tris-HCl, 20 mM EDTA pH = 8.0), heated 2.5 min at 90ºC and snap-chilled in an ice-water bath. The sample was loaded on a 16x16 cm 8M urea - 10% PA – 1xTBE gel, previously pre-run at 250V for 40 min, and run in 1x TBE for 2.7 h at 300V in the dark. Gels were then shaded with an UV lamp to identify the bands corresponding either to labeled or unlabeled RNA. These bands were sliced from the gel, freeze-thawed once and crushed with a tip, and the RNA eluted in 500 μL of 0.3M sodium acetate pH = 5.8 for 2h at 50ºC in the dark. Eluted RNA was precipitated, re-dissolved in RNA storage buffer (*RSB*: 3mM sodium acetate, 0.25 mM EDTA, pH = 6), heated for 2.5 min at 90 ºC and snap-chilled, aliquoted and stored at -80ºC.

### Binding assays with microscale thermophoresis

A frozen aliquot of 0.2 μM Cy5-labeled RNA in RSB was thawed in ice, heated 2.5 min at 90ºC, snap-chilled and kept at 0ºC for 3 min. This denatured RNA was immediately let to fold for 1h at 30ºC in 1x CB with 0.5 mg $mL^{-1}$ BSA at final RNA concentration of 15 nM. The ligand was diluted in 1x CB and then used to prepare serial dilutions with the same buffer, except for the lowest concentration point that contained only the buffer (control). To assemble the binding reactions 8 μL of the folded labeled RNA was mixed with the same volume of the ligand at 25ºC and promptly used to fill up the capillaries for MST measurements. MST measurements were performed using a Monolith NT.115 Green Red MST instrument (Nanotemper technologies, München, Germany) with MST grade standard treated NT.115 capillaries. The MST settings were: temperature of the instrument: 22ºC; LED power: 90%, Red – Ex: 625 nm, Em: 680 nm; IR/MST laser power: 60%; time before heating: 5 sec; time IR/MST on: 30 sec; time after heating: 3 sec. The normalized fluorescence ($F_{norm}$) corresponds to the ratio between the fluorescence measured after the 30 sec period where IR/MST-Laser has been on ($F_{hot}$) divided by the fluorescence measured before the IR/MST-Laser starts heating ($F_{initial}$), i.e. $F_{norm} = F_{hot}/ F_{initial}$. $F_{norm}$ measurements were obtained with NTA Analysis software (NanoTemper Technologies) and normalized ($\Delta F_{norm}$) by subtracting the value of the lowest concentration point (i.e. the only-buffer control). Data were analyzed using GraphPad Prism 5.0, where a non-linear regression (assumptions: one binding-site – specific binding with Hill slope) with the least squares fitting method was used to model binding behavior and the $K_D$.

### Selective 2'-hydroxyl acylation analyzed by primer extension

DNA templates for *in vitro* transcription in SHAPE assays included the T7 promoter, two DNA cassettes to prevent signal loss from C45 (McGinnis et al., 2009), the C45 aptamer sequence, and the first 218 nucleotides of GFP coding sequence. C45 aptamer sequence was first cloned into pWHE601 immediately upstream of ATG initiation codon of GFP (Suess et al., 2003). To this aim, two DNA fragments corresponding to C45 and the linearized plasmid were produced by PCR with primers ADO13 and ADO14, and ADO15 and ADO16, respectively, and assembled using the Gibson Assembly mix (New England Biolabs, Ipswich, MA). pWHE601-C45 was then used as template to generate an amplicon that includes one cassette and C45 using ADO17 and ADO18 primers. In a second PCR, the T7 promoter and the second cassette were included using primers ADO19 and ADO20, and this amplicon was then used as template to generate the final template using ADO21 and ADO20 primers. All PCR reaction were carried out using the Q5® High-Fidelity DNA Polymerase (New England Biolabs) following manufacturer's recommendations. RNA was transcribed *in vitro* and purified as described above.

For RNA folding, a frozen aliquot of unlabeled RNA (diluted in RSB) was thawed in ice, denatured as described above, and then diluted in 1x CB either with or without 86 mM FBP. RNA was let to fold for 1h at 37ºC. 5 pmol of folded RNA was treated with 5 mM 1-methyl-6-nitroisatoic anhydride (1M6, dissolved in anhydrous DMSO) for 3 min at 37ºC, and the reaction quenched with cold 0.3M sodium acetate in ethanol and precipitated. Control samples containing no reagent were prepared in parallel with an equivalent volume of DMSO. For primer extension, RNA pellets (1M6-modified or untreated) were dissolved in 10 μL of RNAse-free $H_2O$ and mixed with 2 μL of a 1.25 μM NED-labeled ADO-22 primer at 5', 4.5 μL of 5x first strand buffer (Invitrogen), 1 μL of 100 mM DTT, 1 μL of dNTPs mix 10 mM, 0.2 μL of RNAse inhibitor and 0.3 μL of SuperScript III reverse transcriptase (Invitrogen). The reaction was carried out for 20 min at 52ºC and quenched at 85ºC for 5 min. Sequencing reactions included 5 pmol of un-modified RNA, 2 μL of 1.25 μM 6-FAM-labeled ADO-22 primer and 1 μl of 100 mM ddTTP (USB-Affymetrix, Cleveland, OH). Fluorescently-labeled cDNA fragments were analyzed by capillary electrophoresis (CE). A sequencing reaction and a sample under study (RNA treated with 1M6 or only DMSO) were loaded in each capillary and analyzed in a 3130xl Genetic Analyzer (Thermo Fisher Sci.) following a prior optimization of the ratio between experimental and sequencing reactions to avoid signal saturation.

To calculate the reactivity values for each nucleotide the electropherograms from CE were processed using QuShape software (Karabiber et al., 2013). In specific, a region of interest was first delimited excluding the final product to prevent signal saturation. Individual peaks were obtained by smoothing the signal and adjusting the baseline in this region. Signal decay correction was omitted. After aligning the peaks from the experimental and control samples, the sequence (provided as input) was aligned to these peaks. The normalized reactivity at each nucleotide position was calculated by dividing each value by the average intensity of the 10% most reactive residues (excluding outliers) (Karabiber et al., 2013). To calculate ligand-induced structural changes (differential shape) the reactivity value at each nucleotide position was subtracted from that in the RNA folded in the presence of FBP. Differences in the reactivity were considered when it was greater than 0.3 and the p-value (t-test, two tails, non-paired) smaller than 0.05.

For the secondary structure predictions, the reactivity values were send to RNA structure software (Reuter et al., 2010), which coupled SHAPE reactivity with energy minimization.

### Quantification of intracellular concentration of fructose-1,6-bisphosphate

3x $10^7$ *TM6** cells from a exponentially-growing culture in minimal medium plus 2.0 g $L^{-1}$ glucose or 2.0 g $L^{-1}$ maltose were quenched in methanol at -80ºC, harvested by centrifugation at 2,500x g for 10 min at -10ºC and the pellet washed with methanol and stored at -80ºC. Extraction of cellular metabolites was done in a solution of methanol, acetonitrile and water (4:4:2 by volume) with 0.1 M formic acid, pre-cooled to -20ºC and with $U^{13}C$ internal standards spiked in. The pellet was extracted twice with 0.9 mL of the solution for 10 minutes at -20ºC with shaking (final volume 1.8 mL). Organic solvents were removed from the supernatant in a vacuum concentrator (2 h, RT), and the remaining water by freeze-drying overnight. The precipitates were resuspended 0.2 mL of water and re-dissolved by vortexing and ultrasonication. Finally, the extract was centrifuged (2 min; 21,000x g,4°C), and 10 μL of the supernatant analyzed using a UHPLC-MS/MS. Quantification was based on the $^{12}C/^{13}C$ peak area ratios related to a calibration curve made of pure $^{12}C$-standards with a global $U^{13}C$-internal standard. The UHPLC-MS/MS system consisted of a Dionex Ultimate 3000 RS UHPLC (Dionex, Germering, Germany). A Waters Acquity UPLC HSS T3 column with precolumn was used at 50°C. A linear binary UHPLC gradient was employed. Quantification was done via multiple reaction monitoring on a MDS Sciex API365 tandem mass spectrometer upgraded to EP10+ (Ionics, Bolton, Ontario, Canada) and equipped with a Turbo-Ionspray source (MDS Sciex, Nieuwerkerk aan den Ijssel, Netherlands). The $^{13}C$ internal standard was prepared by growing *Saccharomyces cerevisiae* on $^{13}C$ uniformly labeled glucose (Cambridge Isotope Labs) as a sole carbon source followed by quenching and metabolite extraction. A detailed description of the UHPLC-MS/MS method and equipment used for LC-MS/MS and preparation of the standards has been previously described (Radzikowski et al., 2016). FBP concentration in each of the 2 biological replicates, which corresponded to the average of independent FBP determinations from two samples of the same culture, was then used to calculate the average FBP-amount per cell.

To determine cell volume we used BudJ (Ferrezuelo et al., 2012), a plugin for ImageJ. In brief, the algorithm determines cell boundaries by detecting two consecutive maximum and minimum pixel values in a densitometric profile along a radial axis from a seed point within the cell, and then fits an ellipse to the boundary pixel array. The measured major and minor axes from the ellipse are utilized to calculate the volume assuming that the cell has the shape of a prolate ellipsoid. At least 70 cells were selected from each biological replicate to calculate the median cell volume. Intracellular FBP concentration for each experiment was calculated by dividing the average FBP-amount per cell by the median of cell volume measurements.

For Figures 6D and 6E, to match the intracellular FBP concentrations with the GFP/mCherry ratios in the wild-type, *HXT7* and *TM6** strains, we implemented the following conversion: $FBP_i^s = mean\ FBP^s \cdot \frac{r_i^s}{mean\ r^s}$, where $FBP_i^s$ is the inferred FBP concentration of the strain *s*'s replicate culture *i* whose GFP/mCherry ratios are shown on the y-axis, *mean* $FBP^s$ is the mean FBP concertation of the strain *s* reported in (Schmidt, 2014), $r_i^s$ is the growth rate in the strain *s*'s replicate culture *i*, and *mean* $r^s$ is the mean growth rate across three replicate of the strain *s*. To infer the intracellular FBP concentration in the *TM3* and *TM4* strains, we used the knowledge that their glucose uptake rates, glycolytic fluxes and growth rates are between the respective values of the *HXT7* and *TM6** strains (Elbing et al., 2004a) and, building on the flux-signaling property of FBP, implemented the conversion: $FBP_i^s = a \cdot r_i^s + b$, where *a* and *b* are the slope and intercept in the linear regression between the mean FBP concentrations and mean growth rates of the *HXT7* and *TM6** strains.

### Determination of GFP/mCherry ratio by flow cytometry

GFP and mCherry fluorescence intensity was measured by flow cytometry (BD Accuri™ C6, Becton Dickinson) at three different time points on the hour scale where cells displayed their normal growth rate. Optical configuration to measure GFP and mCherry signals was 488 nm for excitation and 510/15 BP and 610/20 BP filters, respectively, for detection. Data were analyzed using Kaluza (Beckman Coulter) or Python applied in the same manner. Live cells were first gated by FCS and SSC height parameters, and duplets discarded using SSC width and FSC height parameters. Channels were compensated to remove GFP fluorescence spillover into mCherry signal using the double negative and single-color controls described for cell sorting (see above). GFP/mCherry plots were generated with 20,000 or a specified number of cells of this gate of singlets and live cells, and overlaid with other samples for comparison. To determine the ratio, we exported the compensated raw data from the cells in the main cloud (excluding cells with low mCherry) and calculated single-cell GFP/mCherry values.

### Preparation of C45-HHRz library and HHRz versions for the *in vivo* reporter system

To generate C45-HHRz libraries, and the different HHRz versions used as controls for the calibration of the *in vivo* reporter system, the inserts were amplified by PCR, digested with AvrII and XhoI and ligated to pCS1748 plasmid (Liang et al., 2012), which was previously digested with the same enzymes and de-phosphorylated with Antarctic phosphatase (New England Biolabs). The templates for the inserts of libraries C45-I and II, inv-I and II, and the wild-type satellite RNA of tobacco ringspot virus (sTRSV) HHRz control were generated after five amplification cycles of a SOE PCR, using 10 fmol of each F and R 3'-overlapping denatured primers. The optimal $T_m$ was determined experimentally for each primer pair and a fifth of the volume of this reaction used as template for the amplification of the insert. For libraries sh-I and II and all HHRz-mutant versions we used 0.1 fmol of a unique ssDNA primer as template (ADO41-42 and ADO25-32, respectively). Insert amplification was run for 20 cycles, using 0.5 μM of each primer ADO043 and ADO044 and a $T_m$ of 65ºC. All amplifications were carried out using Q5 polymerase (New England Biolabs) being the PCR protocol set according to manufacturer's recommendation. 100 ng of digested and de-phosphorylated pCS1748 were ligated to a 3-fold molar excess of each digested insert overnight at 16ºC. Six ligation reactions were then pooled and precipitated with 10 μg of glycogen, re-dissolved in 5 μL of $ddH_2O$, transformed into ultracompetent DH5α cells (Inoue et al., 1990) by thermal shock, and the recombinants selected in LB with 100 μg $mL^{-1}$ carbecillin. In these conditions we obtained around 2x$10^5$ clones per library.

To transform the libraries and HHRz versions into the KOY wild-type and *TM6** yeast strains we adapted the LiAc Gietz's transformation protocol (Gietz and Schiestl, 2007) so as to obtain at least as many as 4-fold the maximum theoretical number of clones for each library. In brief, to transform library LibII (containing 7 positions with randomized sequence and a theoretical maximum of 49,152 clones) into *TM6** (displaying a 10-fold lower transformation efficiency than the wild type) we incubated $2x10^{10}$ cells with 18 μg of the plasmid library in 65 mL of a solution of lithium acetate/PEG/denatured salmon sperm carrier DNA (0.1M/33%/0.28mg $mL^{-1}$) in TE pH=7.5 for 45 min at 42ºC. Cells were recovered for 5 hours at 30ºC in YP medium with 2% maltose and then spread onto 50 petri dishes (150x20 mm, Sarstedt) with YNB + CSM $Ura^-$ with 2% maltose supplemented with G418 at 0.2 mg $mL^{-1}$. After 72 hours of incubation more than 200,000 clones (oversampling factor = 4; coverage >98%; (Reetz et al., 2008)) were scrapped from the plates and pooled.

### Sorting of cell subpopulations based on GFP/mCherry ratio by fluorescence-assisted cell sorting

Prior to the sorting each strain had grown for 20 generations in minimal medium without achieving a density higher than $2.5x\ 10^7$ cells $mL^{-1}$ and displayed a constant and reproducible growth rate. Cell density was determined by flow cytometry using an Accuri™ C6 (Becton Dickinson). For each sorting experiment, a double negative (non-transformed strain), and two strains harboring single-color plasmids (GFP, pCS1585) and (mCherry, pCS1749) (Liang et al., 2012) were taken along as compensation controls. In addition, strains harboring the dual-color plasmids with the HHRz versions showing different GFP/mCherry values (HHRz, CTL, and M1 to M7) were also grown in parallel as calibration standards and used to set the sorting gates. All controls were generated in the both KOY wild-type and *TM6** backgrounds. Libraries LibI and LibII were pooled at a proportion of 1:63. Cell cultures were spun down and resuspended to a density of of $5x\ 10^7$ $mL^{-1}$in fresh medium, filtered through a 35 μm cell strainer (BD Falcon), and kept at 4ºC until sorted. Cell sorting was carried out with a MoFlo Astrios (Beckman Coulter) using a 488 nm laser and a 513/26 bandpass emission filter to detect GFP, and a 561 laser and a 614/20 filter to detect mCherry. Live cells were first gated using forward-(FSC) and side-scattered light (SSC) height parameters, then the duplets discarded using SSC width and FSC height parameters, and finally only cells with intermediate mCherry levels within the main cloud were gated. For the pre-selection of C45-HHRz RNA devices with a functional ribozyme we sorted the 3-4% cells with lowest GFP values that did not overlap with the HHRz mutant in the active site (CTL version). For the high-throughput *in vivo* screening of RNA devices the top and bottom sorting gates corresponded to the inactive CTL mutant and the wild-type versions of HHRz, respectively, and the remaining four gates were evenly distributed throughout GFP/mCherry space in between. Sample data were acquired with Summit software (Beckman Coulter). We routinely collected 150,000 cells per sorted sub-populations. For minority subpopulations representing 0.01 to 0.2 % of the input population we collected 2,000 and 20,000 cells, respectively. Sorted cells were collected in 0.5 mL of minimal medium containing either 2% glucose or maltose and 30 μg $mL^{-1}$ chloramphenicol at 4ºC, and then diluted in 7 mL of YNB+CSM $Ura^-$ +2% glucose or maltose and the culture let to grow and passed 1/50 twice.

### Preparation of DNA library for NGS

NGS library was prepared following a three-step PCR amplification scheme: (i) the *outer* PCR, where the region of the plasmid containing the RNA device was amplified, (ii) the *Nextera* PCR, a nested PCR that incorporated universal 5' and 3' tails for Illumina sequencing, and (iii) an indexing PCR to include sample-specific indexes as well as the Illumina adaptors. Plasmids were extracted from a 10 mL culture (5 OD) of sorted cells subpopulations using the Zymoprep™ Yeast Plasmid Miniprep II (Zymo Research) following manufacturer's instructions. Outer PCR was performed with $10^6$ template DNA molecules and 0.5 μM of each ADO47-48 primers for 10 cycles. For nextera PCR, $10^6$ molecules of the amplicons resulting from outer PCR were used as template in a 21 cycle-amplification using 0.5 μM of each ADO50-51 primers. For absolute DNA quantification we used real-time PCR (qPCR). qPCR mix included 0.5 μM of each ADO47-48 (for plasmids) or ADO50-51 primers (for out PCR amplicons), 4 μL of a dilution of the DNA template, and 5 μL of 2x Power SYBR Green PCR Master Mix (Thermo Fisher), and the reaction run for 30 cycles in a CFX Connect™ Real-Time PCR Detection System (Bio-Rad). For absolute quantification, a calibration curve was generated with purified amplicons from pCS1748-CTL HHRz.

A diversity control (Townshend et al., 2015) was spiked into each plasmid preparation (1 molecule of the diversity control per 2,000 of the plasmid) at the point of the outer PCR. It was generated using ADO049 primer as template in an outer PCR amplification, and contained a 17 nucleotide-stretch with a randomized sequence. This kind of control has been previously used to compute the typical number of reads resulting from any single molecule that existed in every sample at that point (Townshend et al., 2015). Here, each outer PCR reaction contained a total of 500 molecules of the diversity control, all of them most likely with a different unique sequence. In addition, we included an additional sample with the plasmid pCS1748-CTL HHRz as a cross-contamination control. All PCR amplifications were carried out with the Q5® High-Fidelity DNA Polymerase (New England Biolabs) following the protocol recommended by the manufacturer, the $T_m$ optimized empirically for each primer pair, and the PCR products purified using the NucleoSpin Gel and PCR Clean-up (Macherey-Nagel). Indexing PCR and NGS were performed by Microsynth (Balgach). In brief, purified products from indexing PCR were quantified using PicoGreen (Thermo Scientific) and pooled together (pooling factor for input samples was 7x, while for the rest of the samples was 1x). The paired-end sequencing was done on Illumina NextSeq 500 mid-output run 150v2 with a capacity of 120 million reads (passed filters), and the reads trimmed and de-replicated prior to our specific analysis.

### Analysis of high-throughput *in vivo* screening (FACS-Seq) of RNA devices

All analysis was performed in Python with the help of the modules *pandas*, *numpy*, *scipy*, *regex*, *matplotlib*, *matplotlib_venn* and *seaborn*. The sequences of the cross-contamination control, diversity control and potential C45-HHRz clones were identified in the NGS data via regular expressions, allowing a small number of matching errors (Table S3). Sequences failing to match these three patterns represented a small proportion of unique sequences (median 1.5e-02) as well as of total coverage (median 1.3e-03), did not show biases to specific samples (Table S4), and were ignored in further analysis. The cross-contamination rate was estimated in all samples and had the low median value of 4.2e-06 (Table S4). Detecting the sequences of diversity control, we verified that a single molecule at the point of the outer PCR was typically supported by two reads in the majority of the samples (Table S4). From the sequences identified as potential C45-HHRz clones (Table S3), the middle part between the primer-binding sites for *Nextera* PCR was extracted and put in a table with the number of corresponding reads (coverage) in every sample. Identical sequences in the table were collapsed, with their coverages summed up. We removed from the table those sequences that did not comply with any of the six RNA-device architectures (Table S3), which amounted to 403 out of the clones covered by at least four reads in both *TM6** replicates on both carbon sources (the fraction of 0.026), 417 out of the clones covered by at least four reads in both wild-type replicates on both carbon sources (the fraction of 0.029) and 742 out of the clones covered by at least two reads in both wild-type replicates on both carbon sources (the fraction of 0.024). Calculation of the measures used for the hit selection (Table S2) was performed in this table. Methods S2 and S3 motivate the choice of coverage thresholds, describe quality controls and present the hit selection in more detail.

### Validation of FBP-sensor candidates

Construction of individual clones identified as sensor candidates in the screening was carried out following the same strategies and experimental conditions as for the preparation of C45-HHRz library (see above). For hits 2_12 and 3_7, we proceeded as for sh libraries using a unique ssDNA primer as template, while for the rest of the constructs we proceeded by SOE PCR with a forward and a reverse primer pair just as we did for C45 or inv libraries. Sequences were verified by Sanger sequencing using ADO77 primer. Plasmids were transformed into KOY wild type, *HXT7*, *TM3*, *TM4* and *TM6** strains using the Lithium acetate/PEG method as described above.

Individual clones were grown in minimal medium as described for the sorting of cell subpopulations (see above), 2 mL in 14-mL round-bottom tubes (Greiner) (Figures 6A–6C) or 10 mL in 100-mL flasks (Figures 6D and 6E). To determine GFP/mCherry ratio, we measured GFP and mCherry by flow cytometry (BD Accuri™ C6, Becton Dickinson) as described above. For each biological replicate experiment (Figure 6A), the *response* of a sensor to the FBP-level difference was calculated as the mean value of the change in the median of single-cell GFP/mCherry ratio values across three time points (see the caption of Figures 6A and 6B). Using the average across the three time points of normal growth is intended for obtaining a robust estimate.

To uncover the dependency of the GFP/mCherry ratio of the sensor 2_6 and mutant 2_6m upon the intracellular FBP concentration in five strains, namely wild type, *HXT7*, *TM3*, *TM4* and *TM6**, we cultivated each of these strains in three replicate cultures provided with 2% glucose as the carbon source. Each of the replicate cultures were propagated in three consecutive exponential cultures, with the data of the latest ones used to make Figures 6D and 6E.

### *In vivo* RNA structural mapping

*In vivo DMS treatment.* 50 mM HEPES-KOH, pH 7.5, was added to a culture sample. Afterwards, we treated cells in the sample by the addition of 100 mM DMS (Sigma Aldrich, cat. D186309), and incubated the sample at 30ºC with moderate shaking for 2 minutes. Next, DTT was added to the final concentration of 0.5 M to quench the reaction, after which the cells were centrifuged at 3,000 g for 2 minutes (4ºC), and the medium discarded. We washed the cells once in ice-cold PBS supplemented with 0.5 M DTT. Pellets were snap-frozen in liquid nitrogen and stored at -80ºC.

*Targeted DMS-MaPseq analysis.* Total RNA was extracted by the addition of TRIzol reagent (ThermoFisher Scientific, cat. 15596018) to cell pellets, followed by the incubation at 60ºC for 30 minutes. RNA purification was performed following manufacturer instructions with minor changes. Briefly, after the addition of 0.2 volumes of chloroform and centrifugation, the upper aqueous phase was added to 2 volumes of 100% ethanol, and then loaded onto an RNA Clean & Concentrator-5 column (Zymo Research, cat. R1013). Before proceeding to the reverse transcription, samples were treated for 30 minutes at 37ºC with 1 U TURBO DNase (ThermoFisher Scientific, cat. AM2238) to remove traces of genomic DNA. Targeted reverse transcription was performed using 100U TGIRT-III (InGex, cat. TGIRT50) in FSB buffer (50 mM Tris-HCl pH 8.3, 75 mM KCl, 3 mM $MgCl_2$]) supplemented with 5 mM DTT, 1 mM dNTPs, 1 μM gene-specific RT primer ADO79, 10 U SuperaseIN RNase Inhibitor (ThermoFisher Scientific, cat. AM2694). Briefly, after mixing RNA with the primer and dNTPs, the sample was heated at 70ºC for 5 minutes and then immediately transferred to ice for 1 minute. After the addition of the remaining components (but TGIRT-III), reactions were further incubated at room temperature for 5 minutes. TGIRT-III was added, and samples were incubated for 2 hours at 57ºC, followed by the addition of 1 μl NaOH 5N and the incubation at 95ºC for 3 minutes to release the cDNA. Samples were then purified on RNA Clean & Concentrator-5 columns and 20% of the eluate was used for targeted PCR amplification (ADO78, ADO79).

PCR amplicons were randomly fragmented to an average size of 150-200 bp using NEBNext dsDNA Fragmentase (New England Biolabs, cat. M0348S), following manufacturer instructions. Samples were then purified using 1 volume of Agencourt AMPure XP beads (Beckman Coulter, cat. A63880) and used as input for library preparation using NEBNext Ultra II DNA Library Prep Kit (New England Biolabs, cat. E7645S), according to manufacturer instructions.

*Data analysis.* Reads were mapped to the respective reference sequences using the rt-map tool of RNA Framework (Incarnato et al., 2018) and Bowtie v2 (Langmead and Salzberg, 2012), after trimming low quality bases (Phred < 20). Per-base mutations and coverage, as well as mutation map (MM) files for spectral deconvolution, were calculated using the rf-count tool (parameters: -na -ni -md 3). Normalized reactivity profiles were computed using the rf-norm tool, by applying box-plot normalization (parameters: -rb AC -n 1000 -sm 4 -nm 3). MM files were instead used as input for DRACO to perform spectral deconvolution of alternative conformations (Morandi et al., 2021).

### Microscopy and image analysis

A cover glass with one (Figures 8C and 8D) or two (Figures 8A and 8B) microfluidic devices was mounted to a Nikon Eclipse Ti-E inverted wide-field fluorescence microscope, where time-lapse imaging of cells was performed. The microscope was equipped with an Andor DU-897 EX camera, a 40x (Nikon CFI Super Fluor 40X Oil; NA = 1.3) and 100x (Nikon CFI Super Fluor 100XS Oil; NA = 0.50-1.30) objectives, as well as a Lumencor AURA excitation system. Imaging was done in four channels. Specifically, in NAD(P)H channel, we excited cells at 360 nm, employing a 350/50-nm band-pass filter, a 409-nm beam-splitter and a 435/40-nm emission filter, while having 2% of the maximal light intensity and 150 ms exposure (the corresponding fluorescence data was not used in the analysis). For GFP measurements, we excited cells at 485 nm, using a 470/40-nm band-pass filter, a 495-nm beam-splitter and a 525/50-nm emission filter, while having 2% of the maximal light intensity and 100 ms exposure (GFP channel). For mCherry measurements, we excited cells at 560 nm, using a 560/40-nm band-pass filter, a 585-nm beam splitter and a 630/75-nm emission filter, while having 2% of the maximal light intensity and 100 ms exposure (mCherry channel). For bright-field imaging, a halogen lamp produced light that was filtered with a 420-nm beam-splitter to exclude UV before illuminating cells (BF channel). The microscopes were operated using NIS-Elements software. We set the Readout Mode to 1 MHz to minimize the camera readout noise and fixed the baseline level of the cameras to 500 at -75 °C. The Nikon Perfect Focus System (PFS) was used in time-lapse imaging to prevent the loss of focus set in the beginning of the experiment. Microscopy imaging of WT strain grown on glucose and *TM6** strain grown on maltose was done with the time steps of 5 minutes, whereas, in case of *TM6** strain grown on glucose, we used the time step of 15 minutes. For Figures 8A and 8B, the 40x objective was used, whereas for Figures 8C and 8D we employed the 100x objective.

In every microscopy experiment, multiple non-overlapping regions in the XY-plane of the microfluidic device(s) were imaged, which resulted in a set of Nikon NIS-Elements ND2 files each containing a multi-channel movie for one XY-region. Every ND2 file was imported into ImageJ (v.1.52n, Java 1.8.0_66) (Schindelin et al., 2009) where images in the bright-field channel were sharpened and contrast-enhanced, after which the movie was saved as a TIFF file. Cells were tracked throughout the movie, and their mother compartments segmented by fitting an ellipse in the bright-field image at each time point via the semi-automated plugin BudJ (Ferrezuelo et al., 2012) used with ImageJ (v.1.49v, Java 1.8.0_144). Simultaneously, by visual inspection and with the help of a custom macro, we recorded for each segmented cell the time points of budding events (appearance of a dark-pixel cluster from which a daughter cell would later grow) and death (abrupt shrinking and darkening of the cell, cessation of cytoplasmic movement, after which the data from the cell was not used). To analyze cellular fluorescence data, we loaded the movie-containing TIFF file into a *NumPy* (v.1.15.4) multidimensional array via Python's module *scikit-image* (v.0.13.1) (van der Walt et al., 2014). For each time point and XY-region, we implemented background-correction by subtracting from every pixel value the mean of 2.5% dimmest pixels in the field of view. We extracted the pixels corresponding to a cell of interest by overlapping the NumPy multidimensional array with the segmentation ellipses provided by BudJ. The fluorescent signal of a cell was defined as the mean value of its background-corrected pixels. To implement cell-autofluorescence correction, for every time point in both GFP and mCherry channels, we calculated the median signal of cells lacking fluorescent proteins, smoothed it using LOWESS regression with 70 data points to fit a local line, and, at the same time point, subtracted the resulting value from the signals of cells expressing the sensor or the mutant. Prior to computing the GFP/mCherry ratio, we smoothed the cell-autofluorescence-corrected GFP and mCherry signals, using LOWESS regression with 8 data points to fit a local line.

## QUANTIFICATION AND STATISTICAL ANALYSIS

For all experiments, the number of replicates, the points and error bars in the plots, the estimated $K_D$ values, and the statistical test and P values, are indicated in the respective figure legends. A description of the analyses performed is detailed in the corresponding experimental sections under method details.